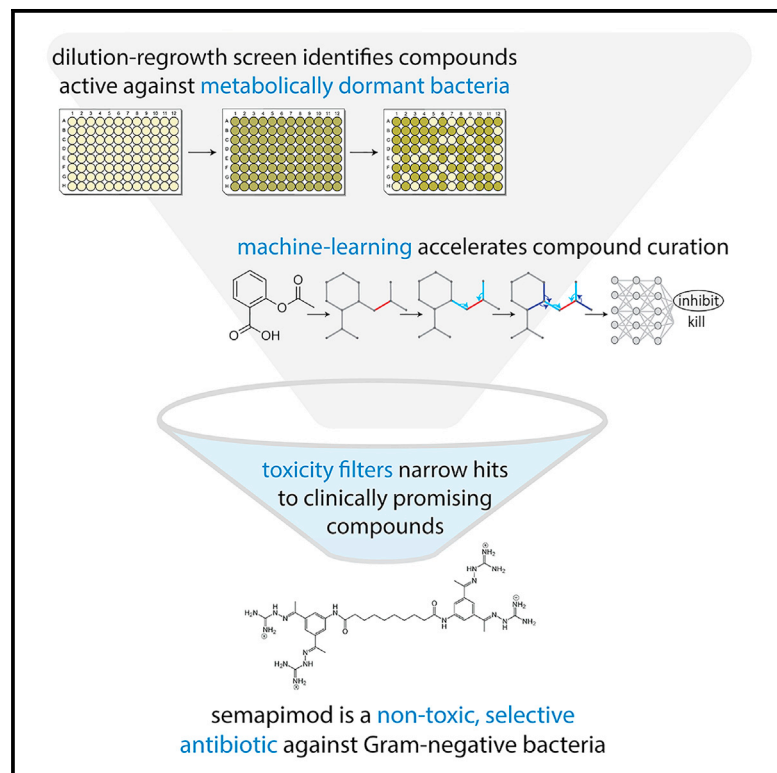


# Cell Chemical Biology

## Discovery of antibiotics that selectively kill metabolically dormant bacteria

### Graphical abstract



### Authors

Erica J. Zheng, Jacqueline A. Valeri, Ian W. Andrews, ..., Lars D. Renner, Sebastian Lourido, James J. Collins

### Correspondence

jimjc@mit.edu

### In brief

Zheng, Valeri, Andrews et al. employ a dilution-regrowth assay and a machine learning (ML) model to identify compounds with activity against stationary-phase bacteria. Semapimod, an anti-inflammatory small molecule with a favorable toxicity profile, demonstrates antibacterial activity against stationary-phase *E. coli* and *A. baumannii* by disrupting the outer membrane.

### Highlights

- Growth inhibition is not synonymous with lethality against stationary-phase *E. coli*
- Experimental screening and machine learning identify lethal compounds
- Toxicity filtering prioritizes antibacterial drugs for further characterization
- Semapimod selectively disrupts the Gram-negative outer membrane



## Article

# Discovery of antibiotics that selectively kill metabolically dormant bacteria

Erica J. Zheng,<sup>1,2,4,10</sup> Jacqueline A. Valeri,<sup>2,3,4,10</sup> Ian W. Andrews,<sup>2,3,10</sup> Aarti Krishnan,<sup>2,3,5</sup> Parijat Bandyopadhyay,<sup>2,3</sup> Melis N. Anahtar,<sup>2,3,4</sup> Alice Herneisen,<sup>5,6</sup> Fabian Schulte,<sup>5</sup> Brooke Linnehan,<sup>5</sup> Felix Wong,<sup>2,3</sup> Jonathan M. Stokes,<sup>7</sup> Lars D. Renner,<sup>8</sup> Sebastian Lourido,<sup>5,6</sup> and James J. Collins<sup>2,3,4,9,11,\*</sup>

<sup>1</sup>Program in Chemical Biology, Harvard University, Cambridge, MA 02138, USA

<sup>2</sup>Infectious Disease and Microbiome Program, Broad Institute of MIT and Harvard, Cambridge, MA 02142, USA

<sup>3</sup>Institute for Medical Engineering & Science, Department of Biological Engineering, and Synthetic Biology Center, Massachusetts Institute of Technology, Cambridge, MA 02139, USA

<sup>4</sup>Wyss Institute for Biologically Inspired Engineering, Harvard University, Boston, MA 02115, USA

<sup>5</sup>Whitehead Institute for Biomedical Research, Cambridge, MA 02142, USA

<sup>6</sup>Department of Biology, MIT, Cambridge, MA 02139, USA

<sup>7</sup>Department of Biochemistry and Biomedical Sciences, McMaster University, Hamilton, Ontario L8N 3Z5, Canada

<sup>8</sup>Leibniz Institute of Polymer Research and the Max Bergmann Center of Biomaterials, 01062 Dresden, Germany

<sup>9</sup>Harvard-MIT Program in Health Sciences and Technology, Cambridge, MA 02139, USA

<sup>10</sup>These authors contributed equally

<sup>11</sup>Lead contact

\*Correspondence: [jimjc@mit.edu](mailto:jimjc@mit.edu)

<https://doi.org/10.1016/j.chembiol.2023.10.026>

## SUMMARY

There is a need to discover and develop non-toxic antibiotics that are effective against metabolically dormant bacteria, which underlie chronic infections and promote antibiotic resistance. Traditional antibiotic discovery has historically favored compounds effective against actively metabolizing cells, a property that is not predictive of efficacy in metabolically inactive contexts. Here, we combine a stationary-phase screening method with deep learning-powered virtual screens and toxicity filtering to discover compounds with lethality against metabolically dormant bacteria and favorable toxicity profiles. The most potent and structurally distinct compound without any obvious mechanistic liability was semapimod, an anti-inflammatory drug effective against stationary-phase *E. coli* and *A. baumannii*. Integrating microbiological assays, biochemical measurements, and single-cell microscopy, we show that semapimod selectively disrupts and permeabilizes the bacterial outer membrane by binding lipopolysaccharide. This work illustrates the value of harnessing non-traditional screening methods and deep learning models to identify non-toxic antibacterial compounds that are effective in infection-relevant contexts.

## INTRODUCTION

Current antibiotic treatment failure rates are unacceptably high, giving rise to chronic and recurrent infections such as those caused by *E. coli* in the urinary tract and *M. tuberculosis* and *P. aeruginosa* in the lung.<sup>1–4</sup> For example, failure rates as high as 16 to 54% are reported for urinary tract infections, causing prolonged or repeated treatment regimens and overall worse health outcomes.<sup>5,6</sup> While some treatment failure can be attributed to genetic resistance, bacteria can also survive antibiotic treatment by adopting metabolically dormant states, which leads to phenotypes known as antibiotic tolerance and persistence.<sup>1,7,8</sup>

Treatment failure associated with tolerance and persistence cannot always be accurately predicted or reproduced in laboratory cultures. This discrepancy can be partially explained by differences in cellular physiology observed in standard microbio-

logical growth conditions versus *in vivo* environments.<sup>9,10</sup> Despite a growing body of evidence suggesting that infectious microenvironments induce bacterial dormancy,<sup>9–11</sup> many traditional antimicrobial susceptibility assays employed in clinical diagnostics and antibiotic discovery are conducted under conditions that sustain high bacterial metabolism and growth.<sup>12,13</sup> Concerningly, many antibiotics that are effective in metabolically active conditions lose efficacy in low metabolic contexts and are vulnerable to the evolution of tolerance.<sup>14–16</sup> There is thus a critical need to identify and characterize antibiotics that are effective under low metabolic conditions that more closely mimic real-world infectious microenvironments.

The discovery of antibacterial compounds with efficacy against dormant cells requires non-traditional screening assays. A typical growth inhibition screen does not inform on lethality, the necessary readout for tolerance and persistence. On the other hand, CFU plating, the gold-standard measure of lethality, is



low-throughput and tedious for large-scale discovery efforts. Dilution-regrowth assays have previously been used as a mid- to high-throughput method for assessing antibiotic lethality. In these assays, a treated culture is diluted into fresh media and re-growth is assessed, with the dilution protocol setting the minimum level of detectable killing.<sup>17–22</sup> However, an ultra-large compound library screen is time- and resource-intensive, particularly on the scales required to expand into new chemical spaces so as to uncover unique antibacterial scaffolds. In response to this challenge, a recent effort from our lab trained a machine learning (ML) model to screen large compound datasets for growth inhibition activity.<sup>23</sup> This ML-enabled virtual screening expanded the available chemical search space, allowing the analysis of substantially more molecules than could be assessed experimentally.

To bring forward antibiotic candidates that are effective against tolerant and persister cells and have true clinical potential, screening efforts should also include toxicity filters in the early discovery phase so as to prioritize compounds that are selectively lethal to bacterial cells over human cells. Previous discovery efforts against tolerant and persister cells have largely identified compounds that non-selectively target cellular membranes or directly cause DNA damage,<sup>24–28</sup> especially when screening for whole-cell phenotypic activity.<sup>29–31</sup> For example, aminoglycosides, mitomycins, and polymyxins, which are all active against non-replicating bacteria, carry considerable toxicity risks for human usage,<sup>25,32,33</sup> and reducing the toxicity of such antibiotics can require re-formulation<sup>34</sup> or potentiation strategies.<sup>35</sup> It has been proposed that many compounds that kill metabolically dormant cells will be inherently toxic to humans because of their more invasive mechanisms of action.<sup>36,37</sup> If so, computational bacterial lethality predictions paired with experimental mammalian cell viability assays may allow us to determine rare counter-examples of antibacterial compounds with favorable toxicity profiles that are effective against dormant bacteria.

Here, we describe a screening pipeline for the discovery of non-toxic antibiotics that kill metabolically dormant bacteria. We implement a dilution-regrowth screen to identify compounds with lethality against metabolically dormant stationary-phase *E. coli*. We pair this screen with ML-driven approaches to expand our search to larger, more diverse chemical spaces. We compare the hits that are enriched in killing versus growth-based screens, highlighting that growth inhibitory activity is not a reliable predictor of lethality. Next, we employ toxicity assays to filter out toxic compounds and to better understand antibiotic properties that are associated with toxicity. We use this pipeline to identify multiple selective compounds that kill metabolically dormant bacteria. Of these compounds, we find that the most potent and structurally distinct compound without any obvious mechanistic liability was semapimod, an anti-inflammatory compound that is bactericidal against dormant *E. coli* and *A. baumannii*, and we show that semapimod binds lipopolysaccharide in the Gram-negative outer membrane as part of its lethality. The discovery approach presented here demonstrates the value of expanding upon traditional screening methods and harnessing both ML-powered virtual screens as well as toxicity filters to identify selective antibacterial compounds that are effective in infection-relevant contexts.

## RESULTS

### A dilution-regrowth screen identifies compounds that kill metabolically dormant *E. coli*

We first implemented a dilution and regrowth-based method for identifying compounds with lethality against metabolically dormant bacteria. Our model system was stationary-phase *E. coli* BW25113 (Ec BW) grown in 1% LB diluted in phosphate-buffered saline (PBS), resulting in a metabolically dormant state that is refractory to killing by conventional antibiotics (Figure S1A) and is a common model for antibiotic-tolerant persister cells.<sup>21,38</sup> Stationary-phase cells were treated for 24 h with compounds, after which a small volume was sub-cultured into fresh, 100% LB media and allowed to re-grow for 24 h (Figures 1A and S1B). After regrowth, optical density readings were normalized and used to identify active “hit” compounds. Using this methodology, we screened the Broad Institute’s Drug Repurposing Hub (DRH) library<sup>39</sup> and detected 111 compounds out of 6,704 that passed our hit threshold in at least one of the two screening replicates (Figure 1B). This lenient initial filtering step, requiring only one active replicate, was used prior to CFU plating. We then validated this set using CFU plating to eliminate false positives where the compound concentration remained above the minimum inhibitory concentration (MIC) during the re-growth stage. From this, we identified 84 compounds (1.3% hit rate) that, at minimum, reduce bacterial load by a factor of 10 (Figure S1C, File S1).

### Growth inhibitory screens are not sufficiently predictive of lethality in metabolically dormant contexts

To understand the intersection between compounds that are effective in metabolically active versus dormant conditions, we simultaneously conducted a traditional growth inhibition screen with the DRH library (Figures 1C and S1D), which resulted in 148 hits (2.2% hit rate) (Figure 1D, File S1). Hits from the dilution-regrowth killing screen were largely a subset of the hits from the growth inhibition screen: 73% of killing hits were also growth inhibitory hits. In contrast, only 41% of growth inhibition hits also had killing activity (Figure 1E). This comparison additionally revealed compounds with killing activity that did not have growth inhibitory activity (27% of killing hits) at the same concentration (Figure 1E).

We further explored the correlation between efficacies in high versus low metabolic states by evaluating whether we could use growth inhibitory data to predict killing activity. We used a trained graph neural network (GNN) model on growth inhibition data from a collection of 2,335 compounds,<sup>23</sup> including FDA-approved drugs and natural products. This model only weakly predicted results from the DRH killing screen, with an area under ROC curve (auROC) of 0.713, area under Precision-Recall curve (auPR) of 0.037 and Matthews Correlation Coefficient (MCC) of 0.052, although it unsurprisingly performed well on the DRH growth inhibition screen (auROC ~0.924, auPR ~0.424, MCC ~0.423) (Figure 1F). These results further support that information about a compound’s growth inhibitory activity is not sufficiently predictive of its killing efficacy in metabolically dormant contexts, highlighting our motivation for identifying compounds with activity in a range of infection-relevant contexts.

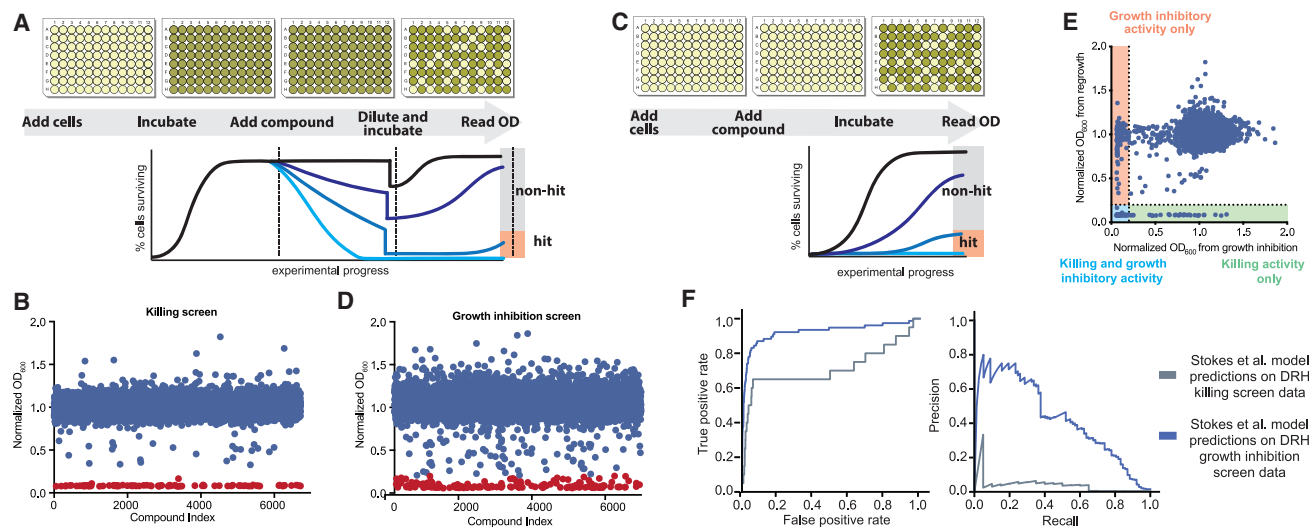


**Figure 1. A dilution-regrowth screen identifies compounds that kill dormant stationary-phase bacteria**

(A) Schematic of the dilution and regrowth-based screening assay to assess killing efficacy against metabolically dormant bacterial cells. An overnight culture of *E. coli* BW25113 (Ec BW) was diluted 1 in 10,000 into 1% LB in PBS, grown to stationary-phase, and treated with antibiotics for 24 h. A small volume was sub-cultured into fresh LB; plates were then incubated for another 24 h and growth (OD<sub>600</sub>) was measured. A cut-off of normalized OD<sub>600</sub> < 0.2 was used to distinguish killing hits from non-hits.

(B) Screening results using the dilution-regrowth screening assay to determine killing of stationary-phase Ec BW with the Drug Repurposing Hub (DRH) library. 111 compounds passed our hit cut-off. Shown are the means of two biological replicates.

(C) Schematic of the growth inhibition screen. An overnight culture of Ec BW was diluted 1 in 10,000 into fresh LB broth, and compound was added. Plates were then incubated for 24 h and OD<sub>600</sub> was measured. A cut-off of normalized OD<sub>600</sub> < 0.2 was used to distinguish growth inhibition hits from non-hits.

(D) Traditional growth inhibition screen carried out on Ec BW with the DRH. 148 compounds passed our hit cut-off. Data are representative of two biological replicates.

(E) Comparison of growth inhibition and killing screens for the DRH library. OD<sub>600</sub> results from the dilution-regrowth killing screen with the DRH library are plotted on the y axis and OD<sub>600</sub> values from the DRH growth inhibition screen are plotted on the x axis.

(F) Performance of the graph neural network (GNN) reported in Stokes et al., 2020<sup>23</sup> on inhibition or killing data from the DRH screens, as evaluated with Receiver-Operating-Characteristic (ROC) curve (left) and Precision-Recall (PR) curve (right).

### Machine learning accelerates compound curation and enriches the killing compound set

To expand our set of lethal compounds, we used our screening data to train a model capable of predicting lethality in a larger, more chemically diverse set of compounds (Figure S2A). Many successful approaches in computational property prediction utilize fixed representations of molecules such as SMILES (Simplified Molecular Input Line Entry System) strings, chemical fingerprints, and feature descriptors.<sup>40</sup> However, models using these fixed vector inputs consistently underperform when compared to representations learned directly from the molecular graph itself,<sup>41,42</sup> i.e., a representation of bonds and atoms as nodes and edges in a graph. These molecular graphs are often fed into GNNs,<sup>43</sup> which are neural networks that convert graph representations into intermediate vector representations. GNNs can be powerful tools for drug property prediction<sup>23,41,44–46</sup> and can accurately predict a compound's properties both one at a time and simultaneously,<sup>41</sup> as reported previously for antibiotic activity.<sup>23</sup>

It is clear from our aforementioned results (Figure 1F) that a GNN model trained on growth inhibition data alone does not adequately capture killing activity against dormant cells, necessitating a new model that incorporates killing data. We first evaluated a GNN trained on both growth inhibition activity and killing activity prediction “tasks,” where the model simultaneously predicts both inhibitory and killing activity for each compound

passed to it as input (Figures 2A and 2B). To benchmark this GNN, we tested simpler models that use chemical fingerprints as input, rather than molecular graphs, such as support vector machines (SVMs). We optimized each model to ensure that all customizable features and parameters were fully tuned to the screening data. After tuning, we found that the GNN was the highest performing model for both inhibition and killing tasks, significantly outperforming all models apart from the inhibition-predicting SVM (Figure 2A).

Given the strong performance of the GNN in our model evaluations, we deployed this model on a database of 799,147 compounds from the Broad Institute. With a modest computing environment, this virtual screen was completed in less than a day, a significantly shorter time than that required for experimental screening. The vast majority of these compounds had low prediction scores for both inhibitory and killing activity (Figure S2B). To prioritize structurally interesting active compounds, we focused on compounds that had predicted killing scores greater than 0.2 and less than 90% structural similarity (Tanimoto similarity) to the training set and a dataset of known antibiotics. We then clustered the remaining 375 compounds into groups of similar structure. These clusters revealed compounds with known killing activity, such as polymyxins<sup>27,47</sup> and antibacterial carbazole analogues<sup>48–50</sup> (Figure 2C), serving as positive controls that the model is able to identify.

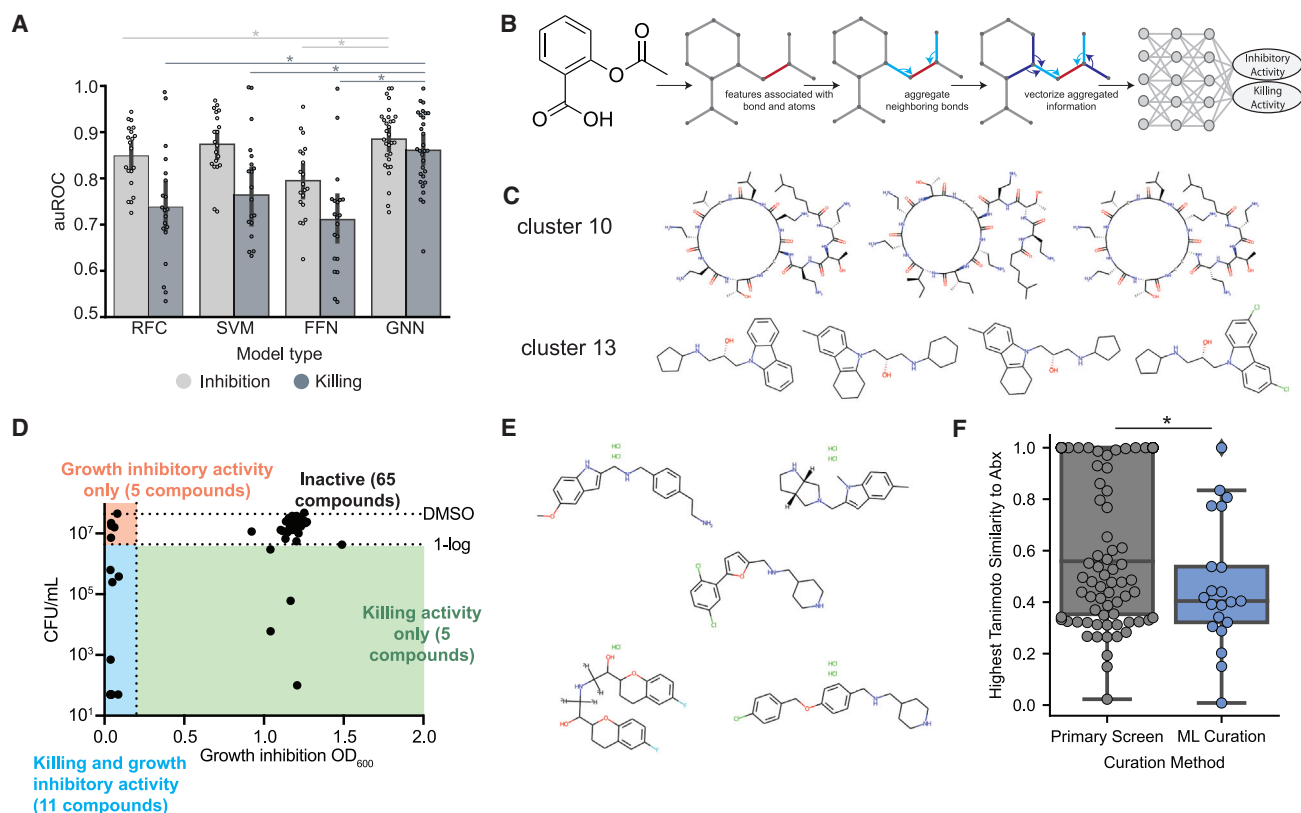


**Figure 2. A multi-task graph neural network (GNN) enriches predictions for compounds with killing activity**

(A) Models that use chemical fingerprints as input are compared to the GNN and evaluated by auROC. The random forest classifier (RFC), support vector machine (SVM), and feedforward neural network (FFN) were evaluated on several 10% test sets held-out from folds with scaffold splits. Each point denotes one model in the ensemble. Asterisks denote significance  $p < 0.05$  with two-sided Mann-Whitney U test.

(B) The multi-task GNN predicts both growth inhibition and stationary-phase killing by aggregating information in neighborhoods of atoms and bonds, shown here as a graph representation of an arbitrary compound (e.g., aspirin).

(C) Predicted high-activity compounds in clusters of similar chemical structure, such as polymyxin-like structures (Cluster 10) and carbazole-containing structures (Cluster 13).

(D) Comparison of killing activity (y axis) and growth inhibitory activity (x axis) of the 86 top-scoring predictions.

(E) Compounds validated to have killing activity from the 36 top-scoring predictions after model retraining and strict similarity and drug-likeness filtering. For this similarity comparison and all following, a more comprehensive set of known antibiotics was used than for the initial antibiotic similarity filtering.

(F) Experimentally validated compounds predicted by the models and compounds identified in the primary screen evaluated on similarity to known antibiotics and antiseptics. ML-curated compounds are derived from both rounds of model prediction on the Broad 800K compound library and larger chemical vendor libraries, respectively. Asterisks denote  $p < 0.05$  with two-sided Mann-Whitney U test.

We experimentally tested the model predictions by curating 86 of the top-scoring compounds (prediction score  $> 0.2$ ), as well as 54 of the lowest-scoring compounds (all with prediction scores  $< 10^{-5}$ ). Notably, 16/86 (19%) of the top-scoring compounds had stationary-phase killing activity, representing a significant enrichment over the 1.3% hit rate observed in the primary DRH killing screen (Figure S2C). In contrast, none of the 54 lowest-scoring compounds had killing activity (Figure S2D). One compound predicted to have killing activity by the model and validated experimentally, SCH-79797, was recently reported as bactericidal against Gram-negative bacteria, including bacterial persisters.<sup>38</sup> Similar to the results from our primary screen, activity in the killing assays was not necessarily a predictor of activity in growth inhibition, and vice versa (Figure 2D).

We next retrained the model with all the available data, including the new validation data. To expand our discovery efforts, we used this model to predict killing activity in a more

diverse chemical space of  $\sim 5$  million commercially available molecules. To reduce re-discovery of known scaffolds, we applied stricter similarity filtering with respect to a manually curated, more comprehensive set of known antibiotics than in our initial screening round. We also applied several filtering steps to identify more “drug-like” compounds, such as Lipinski-conforming compounds and those without PAINS (pan-assay interference compounds) alerts for promiscuous reactivity or Brenk alerts for unfavorable pharmacological properties.

After the aforementioned filtering steps, we curated and tested 36 compounds predicted to have killing activity, finding that five (13.9%) had both growth inhibitory and stationary-phase killing activity (Figure 2E). We note that these validation rates are a conservative estimate of the model’s predictive ability given that we explicitly filtered for compounds that are dissimilar to both the training set and known antibiotics, which is a more difficult test of model generalizability but a more relevant one for antibiotic

discovery. As compounds sharing similar chemical substructures to those of known antibiotics may pass through our similarity filtering step, we computationally verified that the model-predicted compounds were structurally distinct from known antibiotics. We found that these compounds, including the five validated hits, were even more structurally distinct than the compounds found in the primary screen (Figures 2F and S2E). These results demonstrate that iterative model training and compound testing can help identify structurally distinct antibacterial compounds.

### Testing against mammalian cells filters out toxic compounds

After combining our primary DRH killing screen with our ML-powered approach and validation screen, we compiled a total of 105 compounds that kill metabolically dormant bacteria: 84 from the primary screen and 21 from the ML-powered virtual screen. Given the high toxicity of many antibiotics with documented activity against metabolically dormant cells, we designed a three-step toxicity filter with the goal of finding selective compounds that are lethal against metabolically dormant bacterial cells (Figure 3A). We first carried out single-dose cytotoxicity testing against human hepatocellular carcinoma (HepG2) and embryonic kidney (HEK293) cells, with resazurin as a readout of cell viability (Figure 3B). After classifying compounds resulting in less than 50% viability in either cell line as toxic (a lenient initial filtering step) and de-duplicating one compound, we removed 56 compounds from our set of interest, resulting in 49 compounds.

Notably, we found that compounds with low cytotoxicity that were identified by our ML model were, on average, more dissimilar from known antibiotics than compounds with low cytotoxicity identified in the primary screen (Figure 3C). Although we did not filter based on predicted toxicity in our ML approach, this useful finding could result from filtering out compounds with high similarity to active compounds identified in the primary screen, which includes many toxic antiseptics. These observations highlight that computational analyses can enrich for selective compounds that are dissimilar from known antibiotics, thereby helping to identify compounds with varying cytotoxicity and selectivity profiles.

We next investigated the relationship between cytotoxicity and specific antibacterial properties of our hit compounds. We compared the single-point HepG2 viability corresponding to compounds that exhibit growth inhibitory activity against bacterial killing activity (Figure S3A), observing that compounds that are effective at killing dormant cells tend to be more toxic than those that are only effective at growth inhibition. We also studied how antibiotic metabolism dependence relates to cytotoxicity. The majority of our clinically used antibiotics lose efficacy against dormant cells and can be considered “strongly dependent on metabolism” (SDM).<sup>16</sup> To investigate our stationary-phase active compounds, we conducted a high-throughput version of our previously published method for determining metabolic dependence.<sup>16</sup> In brief, this metabolism-dependence assay evaluates survival of cells in both low- and high-nutrient media. Compounds that lose efficacy in low metabolic conditions have positive values of metabolism dependence and vice versa. We found that 18 of our 49 compounds with selective killing activity had metabolism-dependence values of  $\sim 0$ , indicating that they have similar killing efficacy in low and high meta-

bolic conditions and are thus weakly dependent on metabolism (WDM) (Figure 3D). Interestingly, nearly half of the compounds displayed higher killing efficacy in conditions of low metabolism than in conditions of high metabolism, and several of these compounds, including BIX-01294, did not exhibit growth inhibitory activity (Figure S2E). We then plotted HepG2 and HEK293 viability versus metabolism dependence (Figures S3B and S3C), finding that compounds that are only effective in metabolically active contexts tend to have low cytotoxicity, whereas compounds that are effective in metabolically dormant conditions exhibit a range of cytotoxicity profiles. These observations suggest that toxicity is not necessarily an inherent property of these compounds, and that there exist compounds that are active in metabolically dormant contexts which do not cause adverse effects in mammalian cells.

To further study the 49 compounds with low cytotoxicity against HepG2 and HEK293 cells, we estimated the selectivity index for each compound. We performed dose-response measurements for both HepG2 cytotoxicity and stationary-phase bacterial killing and determined the half-maximal inhibitory or effective concentration ( $IC_{50}$ ) in each assay (Figure 3E). Additionally, we only considered compounds that killed more than two logs of bacterial cells in order to focus on compounds with the greatest efficacy, which resulted in the removal of an additional 15 compounds, 14 of which were quinolones. Although quinolones are known to have some efficacy against persister cells depending on dose and SOS response induction,<sup>20,51,52</sup> quinolones target DNA replication, a process essential to dividing cells, and are thus known to be weaker inhibitors of dormant cells. Consistent with this mechanism, the quinolones identified in our set of stationary-phase killing compounds exhibited low killing (approximately 1.5 logs) that barely passed our initial killing hit threshold (Figure S1E). From our dose-response data, we calculated the  $IC_{50}$  for killing stationary-phase Ec BW and for human cell cytotoxicity (Table S1), then divided the human cell  $IC_{50}$  by the bacterial  $IC_{50}$  as a measure of the selectivity index. We proceeded with 15 compounds that had a selectivity index of 4-fold or greater (Figure 3E).

Since many known anti-persister compounds target the bacterial membrane,<sup>24</sup> we directly tested whether our shortlisted compounds disrupt the mammalian cell membrane using a red blood cell hemolysis assay.<sup>53</sup> We found that 11 compounds induced less than 20% hemolysis at 100  $\mu$ M (Figure 3F). Of the 11 compounds, four were polymyxins, compounds which are known to cause nephrotoxicity.<sup>30,54</sup> Additionally, two compounds are known to directly cause DNA damage through either intercalation (acriflavium<sup>55</sup>) or strand breakage (bleomycin<sup>56</sup>). We filtered out these six compounds with known mechanistic liabilities, resulting in five shortlisted compounds.

Lastly, we prioritized the remaining five compounds passing our toxicity filters based on novelty, potency, and potential for *in vivo* efficacy (Table 1). Two of the compounds—bekanamycin and eravacycline—are known antibiotics with anti-persister activity<sup>16,57,58</sup> that are not novel, but validate as positive controls for our discovery and filtering pipeline. Conversely, relatively little is known about the remaining three compounds, semapimod, LTX-315, and BAI1. Semapimod is an experimental

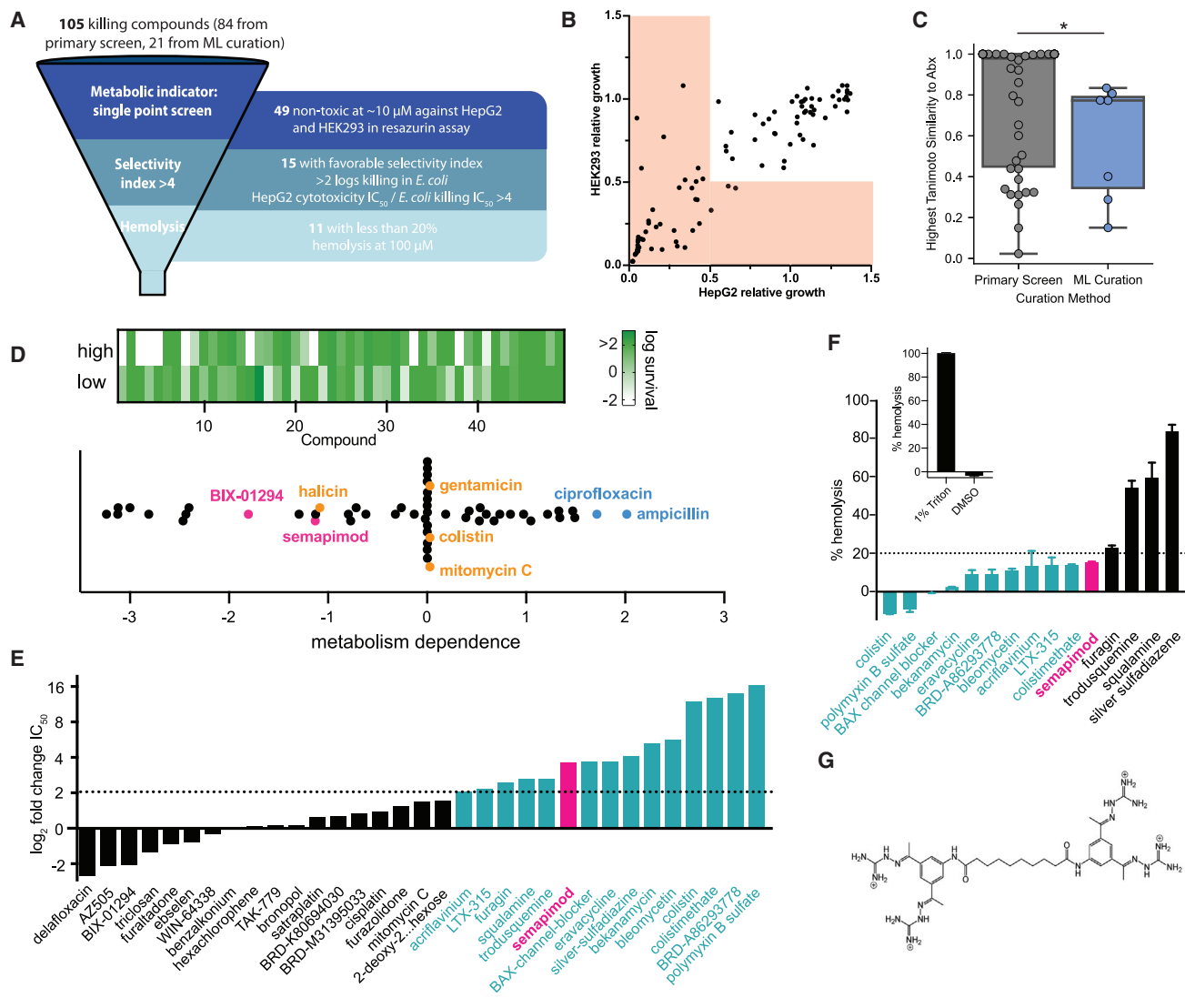


**Figure 3. Toxicity filtering of killing hits highlights semapimod**

(A) Schematic of toxicity filtering steps.

(B) Relative viability of HepG2 and HEK293 in the presence of ~10  $\mu\text{M}$  compound was determined using a resazurin-based cytotoxicity assay. Shown is the mean of two biological replicates. The shaded area indicates a relative viability of <0.5 in either cell line.

(C) Similarity of compounds with >0.5 HepG2 and HEK293 relative viability to known antibiotics and antiseptics. Compounds are separated by their curation method (primary screen or ML). Asterisks denote  $p < 0.05$  with two-sided Mann-Whitney U test.

(D) High-throughput determination of metabolism dependence for the 49 selective stationary-phase killing compounds. (Top) Killing efficacy in low or high metabolic conditions against *Ec BW* at 50  $\mu\text{M}$ . Log survival was calculated by dividing the CFU/mL after antibiotic treatment by the initial CFU/mL to obtain percent survival, and taking the log-transformed value. (Bottom) Metabolism dependence was estimated by dividing the change in cellular survival between high and low metabolic conditions by the change in bacterial intracellular ATP under these conditions,<sup>16</sup> and taking the negative of the resultant value. For comparison, data from known antibiotics are shown. Data are representative of two biological replicates. Negative x axis values indicate less metabolism dependence.

(E) Selectivity index was calculated by dividing the  $\text{IC}_{50}$  of HepG2 relative viability by the  $\text{IC}_{50}$  of *Ec BW* stationary-phase killing. Dose-response curves were performed in biological duplicate. A summary of the  $\text{IC}_{50}$  values can be found in Table S1.

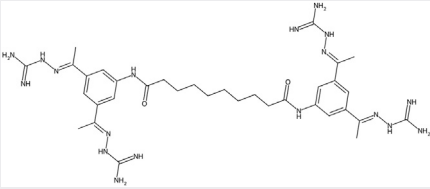
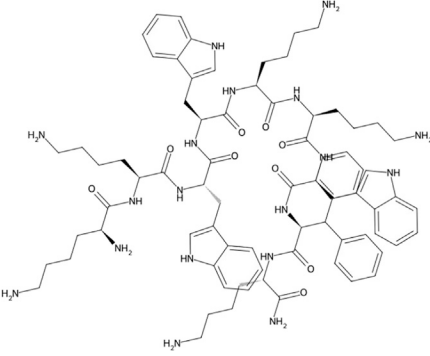
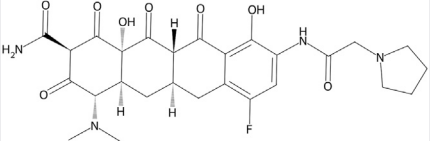
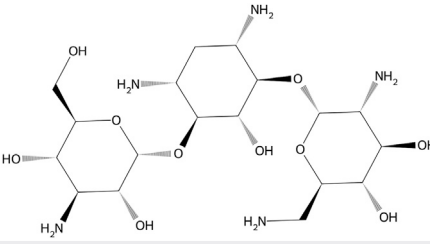
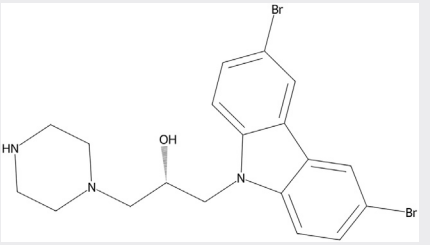
(F) Hemolysis of rat Sprague-Dawley red blood cells was tested at 100  $\mu\text{M}$  compound and normalized to the positive control (1% Triton X-100). Data are representative of two biological replicates; error bars indicate SEM.

(G) Structure of semapimod.

anti-inflammatory drug<sup>59</sup> identified in the primary screen that is the most structurally distinct hit from known antibiotics and possesses the lowest LD99.99, or drug concentration needed to kill 99.99% of bacterial cells, among the remaining compounds. Furthermore, we found that semapimod also retains high killing activity in the presence of serum proteins (Table 1). LTX-315 is

a cationic peptide derived from human lactoferrin that has been investigated as an oncolytic peptide in Phase I clinical trials with an acceptable safety profile.<sup>60,61</sup> BAI1 is a BAX channel blocker that has been explored for its anti-apoptotic properties.<sup>62</sup> LTX-315 and BAI1 both exhibit reduced killing activity in the presence of serum proteins and are less potent (LD99.99)

**Table 1. Five compounds prioritized by the toxicity filtering pipeline**

Compound (description)	Chemical structure	LD99.99 ( $\mu\text{M}$ )	Fold change $\text{IC}_{50}$ with BSA	Tanimoto similarity to most similar known antibiotic
Semapimod (investigational anti-inflammatory drug)		7.43	0.99	0.313
LTX-315 (investigational oncolytic peptide)		11.66	>5	0.796
Eravacycline (tetracycline antibiotic)		21.71	4.04	0.768
Beknamycin (aminoglycoside antibiotic)		21.67	3.59	1.000
BAX inhibitor (BAI1) (apoptosis inhibitor)		100	>5	0.387

LD99.99 is calculated by fitting a four-parameter dose-response curve to the CFU/mL vs. compound concentrations graphs in the presence or absence of 0.55 mM BSA, extracting the Hill slope and  $\text{IC}_{50}$ , and solving for the concentration needed to reduce the bacterial load by 4 log CFU/mL. Tanimoto similarity to most similar known antibiotic is computed with RDKit fingerprints.

than semapimod (Table 1). As semapimod emerged as the most potent and structurally distinct compound without any obvious mechanistic liability, we focused further on elucidating its mechanism of action.

### Semapimod is a non-toxic, selective antibiotic against Gram-negative bacteria

Semapimod passed our toxicity filters with favorable selectivity indexes of 15.6 against HepG2 and 8.5 against HEK293,

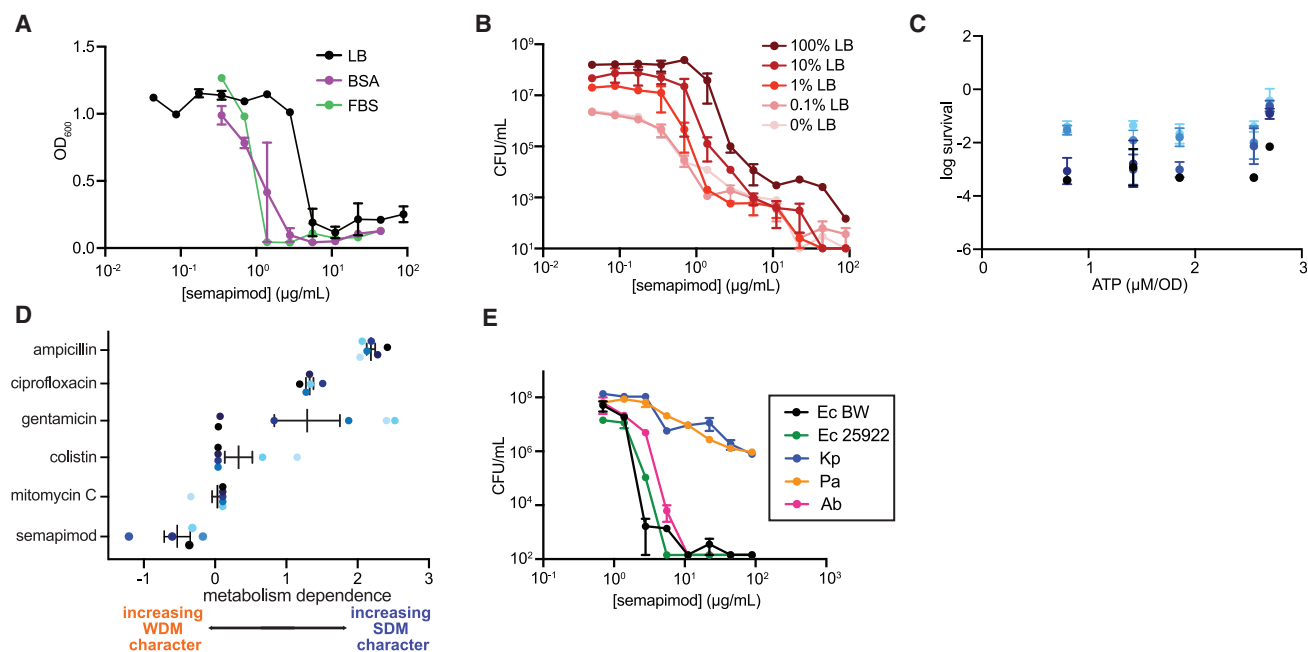


**Figure 4. Semapimod is a non-toxic antibiotic effective against metabolically dormant bacteria**

(A) Semapimod MIC against Ec BW in LB, or in the presence of 0.55 mM BSA or 10% fetal bovine serum (FBS). Data are representative of two biological replicates; error bars represent SEM.

(B) Killing of Ec BW in low to high nutrient conditions. Light red to dark red shading indicates increasing nutrient content.

(C) Survival versus intracellular ATP for concentrations of semapimod at 2X MIC or greater. Light blue to dark blue shading indicates increasing semapimod concentration.

(D) Metabolism dependence of semapimod. Linear regression was performed on the survival versus ATP data, at every antibiotic concentration, and the negative slope was taken as the metabolism-dependence value. Data for known antibiotics are reproduced from Zheng et al., 2020<sup>16</sup> and shown here for comparison. Light blue to dark blue shading indicates increasing antibiotic concentration. Data are representative of two biological replicates; error bars indicate SEM.

(E) Semapimod killing activity against stationary-phase Ec BW, Ec 25922, Kp, Pa, and Ab. Shown is the mean of two biological replicates; error bars represent SEM.

respectively. Importantly, we confirmed that semapimod does not bind to or become sequestered by components of mammalian growth media, as its antibacterial efficacy did not decrease in media containing 10% FBS or BSA (Figure 4A). Semapimod has been investigated as an immunomodulatory drug for Crohn's disease and was well tolerated in clinical trials.<sup>59,63,64</sup> A dose-escalation Phase I clinical trial tested semapimod between 2 and 32 mg/m<sup>2</sup> through intravenous injection over a course of five consecutive days, followed by two additional five-day courses separated by a nine-day rest period.<sup>65</sup> The maximum tolerated dose was not reached, and no negative side effects were reported other than occasional injection-site phlebitis.

While semapimod has been studied for a variety of anti-inflammatory purposes, including in treating Crohn's disease and cancer,<sup>66</sup> its antibacterial properties have not been well investigated. Semapimod is structurally distinct from known antibiotics, with its nearest neighbor being brilacidin, a polymer-based antibiotic (Tanimoto similarity of 0.31). Semapimod also contains several guanylhydrazone motifs, which have previously been shown to possess antibacterial growth inhibitory activity.<sup>67</sup> Additionally, semapimod shares some structural features with pentamidine, which targets the bacterial membrane and potentiates large, hydrophobic antibiotics against Gram-negative bacteria.<sup>68</sup> Pentamidine, however, has no reported bactericidal activity and is much less potent in growth inhibition assays, with an MIC of

100 μg/mL,<sup>68</sup> which is significantly higher than semapimod's MIC of 5 μg/mL.

To further characterize semapimod's antibacterial activity, we first performed a complete metabolism-dependence measurement.<sup>16</sup> We tested semapimod's bactericidal efficacy in a range of media conditions where bacteria are metabolically active or dormant. While most antibiotics lose efficacy in metabolically dormant conditions, we confirmed that semapimod is WDM, as it is effective at killing metabolically active bacteria in addition to metabolically dormant cells (Figures 4B–4D). We next examined semapimod's spectrum of activity, finding that it was highly effective in killing stationary-phase *A. baumannii* (Ab) and a clinical isolate of *E. coli* (Ec 25922), but was less effective (only ~2 logs of killing) against *K. pneumoniae* (Kp) and *P. aeruginosa* (Pa) (Figure 4E). Interestingly, efficacy in stationary-phase killing does not imply antibacterial activity in other contexts. For example, although stationary-phase killing efficacy was similar between Ec BW, Ec 25922, and Ab, semapimod's MIC against Ec BW was ~5 μg/mL, whereas it was ≥100 μg/mL against Ab and Ec 25922 in 100% LB broth (Figure S4A).

#### Semapimod disrupts the bacterial outer membrane as part of its lethality

We sought to understand semapimod's mechanism of action. Motivated by its structural similarity to pentamidine as well as

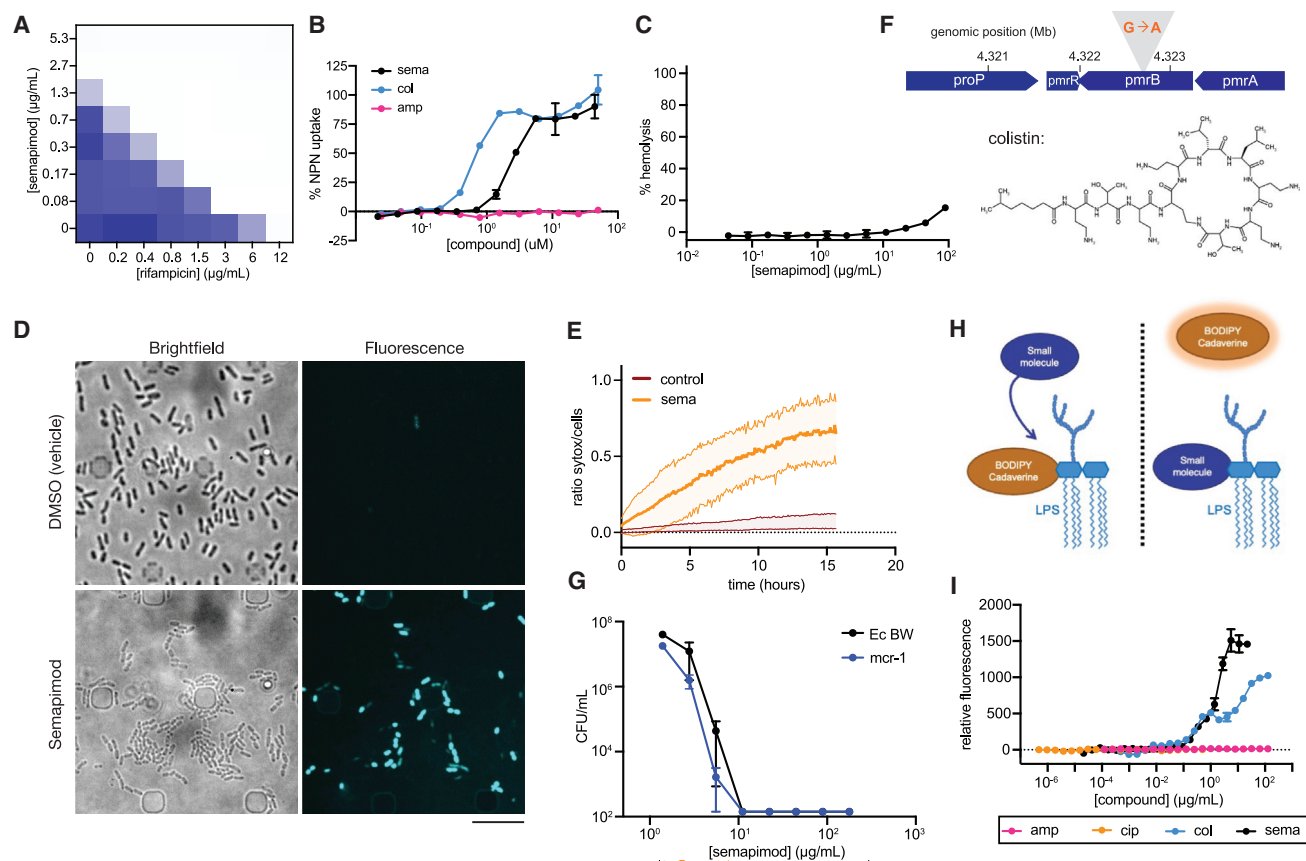


**Figure 5. Semapimod disrupts the bacterial outer membrane by binding LPS**

(A) Growth inhibition checkerboard of Ec BW with semapimod and rifampicin. Darker shading indicates higher bacterial growth. Shown is the mean of two biological replicates.

(B) Uptake of a 1-N-phenyl naphthylamine (NPN) fluorescent probe during semapimod, colistin, and ampicillin treatment in Ec BW. Data are representative of two biological replicates; error bars show SEM.

(C) Semapimod hemolysis was tested against rat Sprague-Dawley red blood cells. Data are representative of two biological replicates; error bars denote SEM. (D) Time-lapse microscopy profiling of semapimod-treated cells. Stationary-phase Ec BW cells were treated with vehicle (DMSO) and semapimod (4X MIC) in the presence of SYTOX Blue, a membrane damage-sensitive dye. Brightfield and fluorescence images of a population of cells 8 h after treatment indicate extensive SYTOX Blue fluorescence in semapimod-treated cells. Results shown are representative of at least 12 different fields of view from three biological replicates, and the total number of cells analyzed was >2,500 per condition. Scale bar denotes 10  $\mu$ m. See also Videos S1, S2, S3, and S4.

(E) Quantification of the fraction of SYTOX-Blue positive cells across all fields of view in the experiments shown in Figure 5C. Thick curves represent average values across all fields of view, and error bars denote standard deviation.

(F) Mutants raised against semapimod have a single-point mutation in the *pmrB* gene, a known colistin-resistance mechanism. The chemical structure of colistin is shown in the inset.

(G) Semapimod killing activity against stationary-phase *E. coli* carrying colistin-resistance determinant *mcr-1* in biological duplicate; error bars denote SEM.

(H) Schematic of LPS binding assay, where displacement of BODIPY-cadaverine from LPS isolated from *E. coli* is monitored by an increase in fluorescence.

(I) BODIPY-cadaverine displacement assay of semapimod binding *E. coli*-derived LPS. Data are representative of two biological replicates; error bars indicate SEM.

its WDM properties, we hypothesized that it targets the bacterial outer membrane. Consistent with this hypothesis, we found that semapimod is synergistic with large, hydrophobic antibiotics, including rifampicin and novobiocin, that are normally excluded by the Gram-negative outer membrane<sup>69,70</sup> (Figures 5A and S4B). Rifampicin and novobiocin are ineffective against Gram-negative bacteria due to their large, hydrophobic structures, and agents that increase bacterial outer membrane permeability are synergistic with these compounds. Furthermore, we found that semapimod was synergistic with rifampicin (FICI < 0.5) against Ec 25922, Kp, and Ab, but not against Pa, possibly due to its more rigid, less

permeable membrane composition<sup>71–73</sup> (Figures S4C–S4F and Table 2).

Measurements of cellular physiology further support that semapimod permeabilizes the outer membrane. We found that 1-N-phenyl naphthylamine (NPN), a hydrophobic fluorescent probe that cannot cross intact outer membranes, is taken up by semapimod-treated cells (Figure 5B). Additionally, a membrane fluidity assay using Laurdan, a lipophilic probe, suggests that semapimod rigidifies the outer membrane (Figure S4G). Indeed, brittle outer membranes are known to be susceptible to breakage and instability.<sup>74,75</sup> Taken together, these findings indicate that semapimod both permeabilizes and rigidifies the outer

**Table 2. Fractional inhibitory concentration index (FICi) for semapimod in combination with rifampicin**

Species	FICi
<i>E. coli</i> BW25113	0.18
<i>P. aeruginosa</i> PAO1	2.00
<i>K. pneumoniae</i> ATCC 13883	0.19
<i>E. coli</i> ATCC 25922	0.06
<i>A. baumannii</i> ATCC 17978	0.08
<i>E. coli</i> BW25113 carrying <i>mcr-1</i>	0.18

Growth inhibition checkerboard assays were performed where an overnight culture was diluted 1 in 10,000 into fresh LB broth, and semapimod and rifampicin were added simultaneously in two-fold gradients to create a concentration checkerboard. An FICi value of less than 0.50 indicates synergy, an FICi value between 0.50 and 4.00 indicates indifference, and an FICi value greater than 4.00 indicates antagonism.

membrane, a mechanism of action similar to that of colistin and other polymyxin antibiotics. It is also important to note that, although semapimod disrupts the bacterial outer membrane, it does not significantly disrupt the mammalian red blood cell membrane to result in hemolysis (Figure 5C).

To probe the effect of semapimod's membrane-targeting mechanism of action on bacterial cell growth, we performed long-term, microfluidic time-lapse microscopy experiments using SYTOX Blue, a DNA-intercalating dye sensitive to membrane damage. Here, single cells with compromised membranes fluoresce throughout the cytoplasm, and the use of microfluidic time-lapse microscopy allows the membrane damage to be spatiotemporally resolved.<sup>76</sup> We found that, as compared to vehicle-treated Ec BW cells, nearly all semapimod-treated cells exhibited persistent increases in SYTOX Blue fluorescence immediately upon treatment, indicating that semapimod robustly damages cellular membranes (Figures 5D and 5E; Videos S1, S2, S3, and S4). Furthermore, these SYTOX Blue-positive cells failed to elongate at timepoints corresponding to the fluorescence intensity increases (Videos S3 and S4). In contrast, cells largely remained SYTOX Blue-negative in vehicle-treated conditions and continually elongated (Videos S1 and S2). This semapimod-induced membrane damage is similar to the membrane damage induced by colistin, which also permeabilizes bacterial membranes.<sup>77–79</sup> Importantly, these observations indicate that bacterial membrane disruption alone is sufficient to explain semapimod's antibacterial activity.

### Semapimod damages bacterial cell membranes by binding lipopolysaccharide

We next sought to further elucidate semapimod's specific outer membrane activity. We first evolved resistance against semapimod in liquid passaging experiments and performed whole-genome sequencing on resistant mutants. We found a single base substitution in the sensor kinase *pmrB* (Figure 5F), a known colistin-resistance mechanism.<sup>80,81</sup> Mutations in *pmrB* cause upregulation of genes responsible for the modification of lipid A with phosphoethanolamine (pEtN) and 4-amino-4-deoxy-L-arabinose (L-Ara4N), which reduce the negative charge on LPS and decrease the electrostatic interaction with positively charged polymyxin antibiotics.<sup>74,80</sup> Here, we found that the identified mutation in *pmrB* was associated with decreases in sema-

mod's growth inhibitory and killing activities (Figures S5A and S5B). Interestingly, although semapimod-resistant cells were cross-resistant to colistin (Figures S5C and S5D), semapimod was still effective at killing *E. coli* carrying the colistin-resistance determinant *mcr-1* (Figure 5G). *mcr-1* encodes a pEtN transferase, which transfers a pEtN moiety onto the negatively charged phosphates on the lipid A portion of LPS, thereby reducing the negative charge on LPS.<sup>74</sup> Although we observed a small (4-fold) increase in the semapimod MIC against *E. coli mcr-1* (Figure S5E), semapimod was still more effective in inhibiting growth than colistin, whose MIC was increased more than 256-fold in the presence of *mcr-1* (Figures S5F and S5G). While semapimod and colistin are both positively charged, it is possible that structural differences allow semapimod to more effectively displace the cations that bridge negatively charged LPS, such that *mcr-1* cells remain vulnerable to semapimod but are resistant to colistin. However, the *pmrB* mutation may fully confer semapimod resistance, as this mutation neutralizes the negative charge on lipid A via both the pEtN and L-Ara4N modifications, which is more effective than only the pEtN modification in *mcr-1* cells.<sup>74</sup>

Although *pmrB* cells were resistant to semapimod, potentiation of rifampicin and novobiocin in the presence of semapimod was still preserved (Figures S5H and S5I). Semapimod was also synergistic with rifampicin and novobiocin in *mcr-1* cells (Figures S5J and S5K). These results are consistent with work demonstrating that *mcr-1* strains are resistant to colistin, but susceptible to outer membrane damage.<sup>82</sup> Moreover, it is known that colistin-resistant strains still display synergy between colistin and other antibiotics like rifampicin, suggesting that the outer membrane permeabilization is not prevented by modifications to LPS.<sup>83,84</sup> While masking of the negative charge on LPS may be sufficient to prevent growth inhibition and killing, it may be insufficient to prevent the binding and disruption of LPS that allows entry of large, hydrophobic antibiotics.

Based on the foregoing results, we hypothesized that semapimod directly binds LPS. Consistent with this hypothesis, we found that semapimod displaces BODIPY-cadaverine conjugated to LPS derived from *E. coli* (Figures 5H and 5I). We additionally used the limulus amoebocyte lysate (LAL) assay to measure LPS endotoxin levels. Our measurements showed that the amount of endotoxin detected in the lysates of semapimod-treated cells decreased as compared to vehicle- and colistin-treated cells (Figure S6A), suggesting that semapimod binds to or sequesters LPS. Furthermore, we found that semapimod activity is sensitive to the dication content of the media, where addition of 21 mM of Mg<sup>2+</sup>, which enhances binding of neighboring LPS molecules, abolished growth inhibition and killing activity (Figures S6B and S6C). However, addition of EDTA, which chelates di-cations and destabilizes the outer membrane, enhanced semapimod activity (Figures S6B–S6E). As LB media contains approximately 30 μM–200 μM of magnesium,<sup>85</sup> we also found that concentrations of Mg<sup>2+</sup> up to 200 μM do not reduce semapimod's killing activity (Figure S6F). A higher concentration of Mg<sup>2+</sup> (1 mM) caused a reduction in killing activity at 10 μM semapimod, but not at 50 μM semapimod (Figure S6F). Human blood Mg<sup>2+</sup> concentrations are typically less than 1 mM,<sup>86</sup> thus, this result does not preclude semapimod's clinical use for systemic infections.

As yet, our observations do not inform on whether semapimod's binding to LPS is specific. To investigate this further, we found that semapimod can also displace BODIPY-cadaverine from LPS derived from *K. pneumoniae* and *P. aeruginosa* with similar potency as with *E. coli* LPS (Figures S6G and S6H). Intriguingly, we note that LPS binding alone is not sufficient for high lethality to *P. aeruginosa* and *K. pneumoniae*, as semapimod killed approximately two logs of these stationary-phase cells at the highest tested concentration (Figure 4E). It is possible that, because the core oligosaccharide of *P. aeruginosa* contains more negatively charged phosphates, an excess of semapimod might be required to disrupt bridging interactions between LPS and dications to destabilize the membrane.<sup>68,87,88</sup> Although semapimod binds free LPS *in vitro* (Figures S6G and S6H), it is also possible that *in vivo* differences in LPS (e.g., O-antigen length or accessibility of phosphates) result in differential susceptibility of *K. pneumoniae* and *P. aeruginosa* to semapimod.<sup>68,89</sup>

Finally, to assess the possibility that semapimod reacts promiscuously with intracellular protein targets, we used thermal proteome profiling (TPP), which identifies protein targets based on their differential heat stability after small molecule binding<sup>38,90–92</sup> (Figure S7A). Across the *E. coli* proteome, the stability of DnaT, RbsA, and HemA was altered by semapimod, suggesting that these proteins (Figures S7B–S7D) may interact with semapimod. Intriguingly, while overexpression of any of these three proteins reduces semapimod lethality, deletion of the non-essential *dnaT* and *rbsA* did not result in altered susceptibility to semapimod, while a deletion of *hemA* could not be tested as it is an essential gene (Figures S7E and S7F). It is possible that overexpression of *dnaT*, *rbsA*, and *hemA* may help sequester semapimod from the intracellular milieu, but that, at physiological concentrations of these proteins and of semapimod, these drug-target interactions are dominated by semapimod's effects on the bacterial cell membrane. This hypothesis is consistent with our finding that semapimod's main mechanism of action is outer membrane disruption, and that outer membrane disruption alone is sufficient for semapimod's lethality against Gram-negative bacteria.

## DISCUSSION

Most commonly used antibiotics were identified during the “golden age” of antibiotic discovery, typically using standard, growth-permissive conditions that elicit high bacterial metabolism.<sup>93</sup> Subsequent research has shown that there is a large diversity of conditions among infectious microenvironments, with many involving nutrient starvation and metabolic dormancy.<sup>9,10,94</sup> Notably, low metabolic states of bacterial pathogens confer tolerance and persistence against many antibiotics that were initially discovered using screening methods that were biased for efficacy in metabolically active contexts, contributing to the difficulty in treating chronic and recurring infections. Motivated by this lack of treatment options, here we have designed a screening pipeline incorporating experimental compound screening, ML-powered virtual screening, and toxicity filters, leading to the identification of multiple antibacterial compounds with favorable toxicity profiles that kill metabolically dormant bacteria.

Our screening pipeline demonstrates the utility of human oversight at all levels of ML workflows.<sup>95</sup> As in previous virtual

screening efforts,<sup>23,96</sup> the intentional choice of training data from a drug repurposing library, a compound set enriched for tolerable ADME properties and compounds with proven antibacterial activity, was important for pre-selecting compounds with translatable properties. Repurposing libraries can benefit drug screening by reducing financial, regulatory, and scientific hurdles in subsequent drug development. Importantly, many clinically approved drugs have acceptably low cytotoxicity.<sup>97</sup> Even among the most toxic drugs in a repurposing dataset, we may expect to see well-documented cytotoxicity reports from animal and human clinical studies, which help to more efficiently prioritize lead candidates.

Although our model identified compounds that are structurally dissimilar from known and clinically used antibiotics (Figures 2E and 2F), many of our discovered compounds have previously reported antibacterial activity. This rediscovery phenomenon, while serving as a useful positive control for our model performance on “real-world” data, underscores the need to diversify and enlarge screening libraries to identify truly novel compounds. As ML models become more sophisticated and are trained on larger datasets, it will be crucial for researchers to remain aware of model biases, limitations, and mistakes.<sup>98</sup> Doing so will inform model generalizability, helping to realize the goal of accelerating compound discovery efforts.

Our screening pipeline resulted in the discovery that semapimod kills metabolically dormant bacterial cells by targeting LPS in the outer membrane. Interestingly, semapimod's anti-inflammatory properties appear to originate from blocking the immune response to LPS in a dose-dependent manner,<sup>59</sup> which may be related to the LPS-binding activity observed here. It is likely that semapimod's selectivity for bacterial membranes is linked to its substantial positive charge, which, similar to other cationic antimicrobials, imparts a high affinity for negatively charged LPS in bacterial membranes over neutrally charged mammalian membranes.<sup>53</sup> Other cationic antibiotics such as colistin also target the bacterial membrane and are effective against metabolically dormant cells; however, these compounds have clinical toxicity concerns,<sup>99–101</sup> and it was therefore surprising that semapimod has proven human safety in clinical trials. Although metabolism dependence and toxicity are correlated (Figure S3), our work demonstrates that toxicity is not necessarily an inherent property of antibacterial compounds that kill metabolically dormant bacterial cells.

Despite their similar mechanisms of action, semapimod and colistin can be differentiated by their spectrum of activity. While colistin is effective against most Gram-negative bacteria,<sup>102</sup> semapimod has narrow-spectrum activity that varies with biological context. Semapimod's spectrum of activity against stationary-phase bacteria is broader in nutrient-poor media than against growing bacteria in nutrient-rich media. Although antibiotics that are effective against metabolically active cells commonly lose activity in metabolically dormant conditions, cases of the opposite are rare. Importantly, the differences in semapimod's activity in our experimental models of these contexts do not arise from changes in magnesium concentration alone (Figure S6F). Semapimod's context-dependent activity may be attributed to an increase in the amount of exposed LPS on the bacterial outer membrane in stationary phase,<sup>103,104</sup> which could in turn increase the electrostatic attraction between semapimod's positively charged

guanyldihydrazone moieties and the negatively charged LPS. Although further characterization is needed to better understand the mechanistic aspects of LPS binding, semapimod's potent, narrow-spectrum efficacy in killing metabolically dormant *E. coli* and *A. baumannii* cells makes it a promising candidate for additional pre-clinical studies.

Future studies may consider explicitly screening for activity against Gram-negative bacterial membranes. The Gram-negative outer membrane is a selective filter that undermines many available antibacterials,<sup>69,105</sup> and membrane-targeting antibiotics may be beneficial for potentiating these drugs. In fact, Silver<sup>106</sup> has suggested that Gram-negative antibiotic discovery is limited more by targeting of the outer membrane than by target discovery. As membrane-active antibiotics target a conserved feature of bacterial cells, their usage might also lead to less resistance, and these antibiotics might robustly maintain their activity against persister cells.<sup>36</sup> It is also important to note that, as a consequence of targeting the membrane, bacterial cell lysis may be expected to occur. This is similar to the cell death phenotypes induced by other antibiotics, such as beta-lactams,<sup>107</sup> and might lead to similar pro-inflammatory immune responses in patients.<sup>108</sup> Additionally, membrane-targeting antibiotics may be cytotoxic due to the similarities between bacterial and human cell membranes, with some exceptions such as semapimod. Counter-screening for cytotoxicity in human cell lines (Figure 3B), as well as red blood cell hemolysis (Figure 5C), can help to identify selective compounds.<sup>36</sup>

It is worth considering whether the growth-based strategies that have been used for antibiotic discovery in the past may have biased the therapeutics that are selected for clinical development.<sup>109,110</sup> Future antibiotic discovery efforts should aim to explore the full scope of bacterial physiologies that are clinically relevant, encompassing both growth-permissive and metabolically dormant conditions, in addition to the intersections of these two biological contexts. Our work demonstrates the value of integrating non-traditional screening methods with ML models to identify non-toxic antibiotics that are effective against metabolically dormant bacteria, which paves the way for more effectively treating chronic and recurrent infections.

### Limitations of the study

Here, we show that a dilution-regrowth assay and computational techniques can efficiently identify antibacterial drugs active against stationary-phase bacteria. The dilution-regrowth assay is a high-throughput and imperfect filter; 84 out of 111 drugs identified in the high-throughput screen had activity when measured with gold-standard CFU plating, indicating that the dilution-regrowth screen has ~24% false positive rate. Secondly, our toxicity filtering pipeline does not cover all possible mechanisms of toxicity but instead focuses on some of the most relevant toxicity liabilities for clinical use, i.e., liver and kidney cell toxicity and red blood cell hemolysis. Additional cell line screening and computational toxicity modeling would more comprehensively assess the translational potential of our candidate drugs. Finally, our characterization of semapimod's mechanism does not extend to *in vivo* evaluation. We posit that semapimod binds the LPS of Gram-negative cell membranes *in vivo* to effect killing of stationary-phase *E. coli* and *A. baumannii*, but

we cannot know with certainty that this mechanism translates from an *in vitro* context to a clinical setting.

### SIGNIFICANCE

**This work highlights how non-traditional screening techniques can identify antibacterial small molecules with relevance for clinical settings. Building on prior work establishing that bacterial metabolism can affect drug efficacy, we evaluate small molecules that have lethality against stationary-phase *E. coli*. We demonstrate that a dilution-regrowth screening technique and machine learning for molecular property prediction can enhance antibacterial drug discovery efforts. We report the antibacterial activity of semapimod, a previously described anti-inflammatory small molecule, and show that semapimod affects its killing activity by binding lipopolysaccharide in the Gram-negative outer membrane.**

### STAR★METHODS

Detailed methods are provided in the online version of this paper and include the following:

- KEY RESOURCES TABLE
- RESOURCE AVAILABILITY
  - Lead contact
  - Materials availability
  - Data and code availability
- EXPERIMENTAL MODEL AND STUDY PARTICIPANT DETAILS
- METHOD DETAILS
  - Dilution-regrowth screen to assess stationary-phase lethality
  - Stationary-phase killing colony forming unit determination
  - Growth inhibition screen
  - Growth inhibitory model on new screening data
  - Data pre-processing for model training
  - Model architecture and training
  - Shallow model comparison
  - Model deployment
  - Antibiotic compound curation
  - Retraining model with validation data
  - Retrained model deployed on more diverse chemical datasets
  - Generation of t-SNE
  - Resazurin-based cytotoxicity assays
  - Determination of metabolism dependence
  - Determination of IC<sub>50</sub>, LD99.99, and selectivity index
  - Red blood cell hemolysis assay
  - Growth inhibition and checkerboard assays
  - NPN membrane permeabilization assay
  - Laurdan membrane fluidity assay
  - Microfluidic imaging
  - Semapimod evolution protocol
  - BODIPY-cadaverine displacement assay
  - Endotoxin binding assay
  - Thermal proteome profiling (TPP)
- QUANTIFICATION AND STATISTICAL ANALYSIS

## SUPPLEMENTAL INFORMATION

Supplemental information can be found online at <https://doi.org/10.1016/j.chembiol.2023.10.026>.

## ACKNOWLEDGMENTS

We thank Angela Koehler for helpful discussions and suggestions. This work was supported by NIH grant R01-AI146194, DTRA grant HDTRA-12210032, the Broad Institute of MIT and Harvard, a fellowship to I.W.A. from the NSF Graduate Research Fellowship Program (1122374), and a fellowship to J.A.V. from the MIT-Takeda Program. A.K. was supported by the Swiss National Science Foundation under grant number SNSF\_203071. A.H. was supported by award 174530 from the National Science Foundation. S.L. was supported by NIH grant R01-AI144369. L.D.R. was supported by the Volkswagen Foundation. F.W. was supported by the NIAID of the NIH under award number K25AI168451 and the James S. McDonnell Foundation. This work is part of the Antibiotics-AI Project, which is directed by J.J.C. and supported by the Audacious Project, Flu Lab, LLC, the Sea Grape Foundation, Rosamund Zander and Hansjorg Wyss for the Wyss Foundation, and an anonymous donor.

## AUTHOR CONTRIBUTIONS

Conceptualization, E.J.Z., J.A.V., I.W.A., J.M.S., and J.J.C.; Methodology, E.J.Z., J.A.V., I.W.A., and F.W.; Screen development and execution, E.J.Z., J.A.V., and I.W.A.; Semapimod mechanistic characterization, E.J.Z., J.A.V., I.W.A., A.K., P.B., M.N.A., F.W.; Thermal proteome profiling, A.K., A.H., F.S., B.L., S.L.; Microscopy, F.W. and L.D.R.; Manuscript writing, E.J.Z., J.A.V., and I.W.A.; Manuscript review and editing, all authors. Funding acquisition, J.J.C.; Supervision, J.J.C.

## DECLARATION OF INTERESTS

J.J.C. is a scientific co-founder and scientific advisory board chair of EnBiotix, an antibiotic drug discovery company, and PhareBio, a non-profit social venture for antibiotic drug discovery. J.M.S. is a scientific co-founder and scientific director at PhareBio.

Received: November 29, 2022

Revised: August 13, 2023

Accepted: October 30, 2023

Published: November 28, 2023

## REFERENCES

- Grant, S.S., and Hung, D.T. (2013). Persistent bacterial infections, antibiotic tolerance, and the oxidative stress response. *Virulence* 4, 273–283. <https://doi.org/10.4161/viru.23987>.
- Blango, M.G., and Mulvey, M.A. (2010). Persistence of Uropathogenic *Escherichia coli* in the Face of Multiple Antibiotics. *Antimicrob. Agents Chemother.* 54, 1855–1863. <https://doi.org/10.1128/AAC.00014-10>.
- Mulcahy, L.R., Burns, J.L., Lory, S., and Lewis, K. (2010). Emergence of *Pseudomonas aeruginosa* Strains Producing High Levels of Persister Cells in Patients with Cystic Fibrosis. *J. Bacteriol.* 192, 6191–6199. <https://doi.org/10.1128/JB.01651-09>.
- Dengler Haunreiter, V., Boumasmoud, M., Häffner, N., Wipfli, D., Leimer, N., Rachmühl, C., Kühnert, D., Achermann, Y., Zbinden, R., Benussi, S., et al. (2019). In-host evolution of *Staphylococcus epidermidis* in a pacemaker-associated endocarditis resulting in increased antibiotic tolerance. *Nat. Commun.* 10, 1149. <https://doi.org/10.1038/s41467-019-09053-9>.
- Lawrenson, R.A., and Logie, J.W. (2001). Antibiotic failure in the treatment of urinary tract infections in young women. *J. Antimicrob. Chemother.* 48, 895–901. <https://doi.org/10.1093/jac/48.6.895>.
- Karve, S., Ryan, K., Peeters, P., Baelen, E., Rojas-Farreras, S., Potter, D., and Rodríguez-Baño, J. (2018). The impact of initial antibiotic treatment failure: Real-world insights in patients with complicated urinary tract infection. *J. Infect.* 76, 121–131. <https://doi.org/10.1016/j.jinf.2017.11.001>.
- Santi, I., Manfredi, P., Maffei, E., Egli, A., and Jenal, U. (2021). Evolution of Antibiotic Tolerance Shapes Resistance Development in Chronic *Pseudomonas aeruginosa* Infections. *mBio* 12, e03482-20. <https://doi.org/10.1128/mBio.03482-20>.
- Fauvart, M., De Groote, V.N., and Michiels, J. (2011). Role of persister cells in chronic infections: clinical relevance and perspectives on anti-persister therapies. *J. Med. Microbiol.* 60, 699–709. <https://doi.org/10.1099/jmm.0.030932-0>.
- Meylan, S., Andrews, I.W., and Collins, J.J. (2018). Targeting Antibiotic Tolerance, Pathogen by Pathogen. *Cell* 172, 1228–1238. <https://doi.org/10.1016/j.cell.2018.01.037>.
- Bjarnsholt, T., Whiteley, M., Rumbaugh, K.P., Stewart, P.S., Jensen, P.Ø., and Frimodt-Møller, N. (2022). The importance of understanding the infectious microenvironment. *Lancet Infect. Dis.* 22, e88–e92. [https://doi.org/10.1016/S1473-3099\(21\)00122-5](https://doi.org/10.1016/S1473-3099(21)00122-5).
- Liu, Y., Tan, S., Huang, L., Abramovitch, R.B., Rohde, K.H., Zimmerman, M.D., Chen, C., Dartois, V., VanderVen, B.C., and Russell, D.G. (2016). Immune activation of the host cell induces drug tolerance in *Mycobacterium tuberculosis* both *in vitro* and *in vivo*. *J. Exp. Med.* 213, 809–825. <https://doi.org/10.1084/jem.20151248>.
- Khan, Z.A., Siddiqui, M.F., and Park, S. (2019). Current and Emerging Methods of Antibiotic Susceptibility Testing. *Diagnostics* 9, 49. <https://doi.org/10.3390/diagnostics9020049>.
- Humphries, R.M., Ambler, J., Mitchell, S.L., Castanheira, M., Dingle, T., Hindler, J.A., Koeth, L., and Sei, K.; CLSI Methods Development and Standardization Working Group of the Subcommittee on Antimicrobial Susceptibility Testing (2018). CLSI Methods Development and Standardization Working Group Best Practices for Evaluation of Antimicrobial Susceptibility Tests. *J. Clin. Microbiol.* 56, e01934-17. <https://doi.org/10.1128/JCM.01934-17>.
- Zheng, E.J., Andrews, I.W., Grote, A.T., Manson, A.L., Alcantar, M.A., Earl, A.M., and Collins, J.J. (2022). Modulating the evolutionary trajectory of tolerance using antibiotics with different metabolic dependencies. *Nat. Commun.* 13, 2525. <https://doi.org/10.1038/s41467-022-30272-0>.
- Lopatkin, A.J., Stokes, J.M., Zheng, E.J., Yang, J.H., Takahashi, M.K., You, L., and Collins, J.J. (2019). Bacterial metabolic state more accurately predicts antibiotic lethality than growth rate. *Nat. Microbiol.* 4, 2109–2117. <https://doi.org/10.1038/s41564-019-0536-0>.
- Zheng, E.J., Stokes, J.M., and Collins, J.J. (2020). Eradicating Bacterial Persisters with Combinations of Strongly and Weakly Metabolism-Dependent Antibiotics. *Cell Chem. Biol.* 27, 1544–1552.e3. <https://doi.org/10.1016/j.chembiol.2020.08.015>.
- Brauner, A., Shores, N., Fridman, O., and Balaban, N.Q. (2017). An Experimental Framework for Quantifying Bacterial Tolerance. *Biophys. J.* 112, 2664–2671. <https://doi.org/10.1016/j.bpj.2017.05.014>.
- Sutton, S. (2010). The Most Probable Number Method and Its Uses in Enumeration, Qualification, and Validation. *J. Val Technol.* 16, 35–38.
- Niu, H., Cui, P., Shi, W., Zhang, S., Feng, J., Wang, Y., Sullivan, D., Zhang, W., Zhu, B., and Zhang, Y. (2015). Identification of Anti-Persister Activity against Uropathogenic *Escherichia coli* from a Clinical Drug Library. *Antibiotics (Basel)* 4, 179–187. <https://doi.org/10.3390/antibiotics4020179>.
- Niu, H., Cui, P., Yee, R., Shi, W., Zhang, S., Feng, J., Sullivan, D., Zhang, W., Zhu, B., and Zhang, Y. (2015). A Clinical Drug Library Screen Identifies Tosufloxacin as Being Highly Active against *Staphylococcus aureus* Persisters. *Antibiotics (Basel)* 4, 329–336. <https://doi.org/10.3390/antibiotics4030329>.
- Kim, J.-S., Heo, P., Yang, T.-J., Lee, K.-S., Cho, D.-H., Kim, B.T., Suh, J.-H., Lim, H.-J., Shin, D., Kim, S.-K., and Kweon, D.H. (2011). Selective killing of bacterial persisters by a single chemical compound without affecting normal antibiotic-sensitive cells. *Antimicrob. Agents Chemother.* 55, 5380–5383. <https://doi.org/10.1128/AAC.00708-11>.

22. Liebens, V., Defraigne, V., Knapen, W., Swings, T., Beullens, S., Corbau, R., Marchand, A., Chaltin, P., Fauvart, M., and Michiels, J. (2017). Identification of 1-((2,4-Dichlorophenethyl)Amino)-3-Phenoxypropan-2-ol, a Novel Antibacterial Compound Active against Persisters of *Pseudomonas aeruginosa*. *Antimicrob. Agents Chemother.* *61*, e00836-17. <https://doi.org/10.1128/AAC.00836-17>.
23. Stokes, J.M., Yang, K., Swanson, K., Jin, W., Cubillos-Ruiz, A., Donghia, N.M., MacNair, C.R., French, S., Carfrae, L.A., Bloom-Ackermann, Z., et al. (2020). A Deep Learning Approach to Antibiotic Discovery. *Cell* *180*, 688–702.e13. <https://doi.org/10.1016/j.cell.2020.01.021>.
24. Defraigne, V., Fauvart, M., and Michiels, J. (2018). Fighting bacterial persistence: Current and emerging anti-persister strategies and therapeutics. *Drug Resist. Updates* *38*, 12–26. <https://doi.org/10.1016/j.drug.2018.03.002>.
25. Kwan, B.W., Chowdhury, N., and Wood, T.K. (2015). Combatting bacterial infections by killing persister cells with mitomycin C. *Environ. Microbiol.* *17*, 4406–4414. <https://doi.org/10.1111/1462-2920.12873>.
26. Chowdhury, N., Wood, T.L., Martínez-Vázquez, M., García-Contreras, R., and Wood, T.K. (2016). DNA-crosslinker cisplatin eradicates bacterial persister cells. *Biotechnol. Bioeng.* *113*, 1984–1992. <https://doi.org/10.1002/bit.25963>.
27. Grassi, L., Di Luca, M., Maisetta, G., Rinaldi, A.C., Esin, S., Trampuz, A., and Batoni, G. (2017). Generation of Persister Cells of *Pseudomonas aeruginosa* and *Staphylococcus aureus* by Chemical Treatment and Evaluation of Their Susceptibility to Membrane-Targeting Agents. *Front. Microbiol.* *8*, 1917.
28. Schrank, C.L., Wilt, I.K., Montegudo Ortiz, C., Haney, B.A., and Wuest, W.M. (2021). Using membrane perturbing small molecules to target chronic persistent infections. *RSC Med. Chem.* *12*, 1312–1324. <https://doi.org/10.1039/D1MD00151E>.
29. Farha, M.A., and Brown, E.D. (2015). Unconventional screening approaches for antibiotic discovery. *Ann. N. Y. Acad. Sci.* *1354*, 54–66. <https://doi.org/10.1111/nyas.12803>.
30. Ordoeí Javan, A., Shokouhi, S., and Sahraei, Z. (2015). A review on colistin nephrotoxicity. *Eur. J. Clin. Pharmacol.* *71*, 801–810. <https://doi.org/10.1007/s00228-015-1865-4>.
31. Verweij, J., and Pinedo, H.M. (1990). Mitomycin C: mechanism of action, usefulness and limitations. *Anti Cancer Drugs* *1*, 5–13.
32. Prokhorova, I., Altman, R.B., Djumagulov, M., Shrestha, J.P., Urzhumtsev, A., Ferguson, A., Chang, C.-W.T., Yusupov, M., Blanchard, S.C., and Yusupova, G. (2017). Aminoglycoside interactions and impacts on the eukaryotic ribosome. *Proc. Natl. Acad. Sci. USA* *114*, E10899–E10908. <https://doi.org/10.1073/pnas.1715501114>.
33. Lim, L.M., Ly, N., Anderson, D., Yang, J.C., Macander, L., Jarkowski, A., Forrest, A., Bullitta, J.B., and Tsuji, B.T. (2010). Resurgence of Colistin: A Review of Resistance, Toxicity, Pharmacodynamics, and Dosing. *Pharmacotherapy* *30*, 1279–1291. <https://doi.org/10.1592/phco.30.12.1279>.
34. Lam, A.K., Moen, E.L., Pusavat, J., Wouters, C.L., Panlilio, H., Ferrell, M.J., Houck, M.B., Glatzhofer, D.T., and Rice, C.V. (2020). PEGylation of Polyethylenimine Lowers Acute Toxicity while Retaining Anti-Biofilm and  $\beta$ -Lactam Potentiation Properties against Antibiotic-Resistant Pathogens. *ACS Omega* *5*, 26262–26270. <https://doi.org/10.1021/acso-mega.0c04111>.
35. Rosenberg, C.R., Fang, X., and Allison, K.R. (2020). Potentiating aminoglycoside antibiotics to reduce their toxic side effects. *PLoS One* *15*, e0237948. <https://doi.org/10.1371/journal.pone.0237948>.
36. Hurdle, J.G., O'Neill, A.J., Chopra, I., and Lee, R.E. (2011). Targeting bacterial membrane function: an underexploited mechanism for treating persistent infections. *Nat. Rev. Microbiol.* *9*, 62–75. <https://doi.org/10.1038/nrmicro2474>.
37. Payne, D.J., Gwynn, M.N., Holmes, D.J., and Pompliano, D.L. (2007). Drugs for bad bugs: confronting the challenges of antibacterial discovery. *Nat. Rev. Drug Discov.* *6*, 29–40. <https://doi.org/10.1038/nrd2201>.
38. Martin, J.K., Sheehan, J.P., Bratton, B.P., Moore, G.M., Mateus, A., Li, S.H.-J., Kim, H., Rabinowitz, J.D., Typas, A., Savitski, M.M., et al. (2020). A Dual-Mechanism Antibiotic Kills Gram-Negative Bacteria and Avoids Drug Resistance. *Cell* *181*, 1518–1532.e14. <https://doi.org/10.1016/j.cell.2020.05.005>.
39. Corsello, S.M., Bittker, J.A., Liu, Z., Gould, J., McCarren, P., Hirschman, J.E., Johnston, S.E., Vrcic, A., Wong, B., Khan, M., et al. (2017). The Drug Repurposing Hub: a next-generation drug library and information resource. *Nat. Med.* *23*, 405–408. <https://doi.org/10.1038/nm.4306>.
40. Elton, D.C., Boukouvalas, Z., Fuge, M.D., and Chung, P.W. (2019). Deep learning for molecular design—a review of the state of the art. *Mol. Syst. Des. Eng.* *4*, 828–849. <https://doi.org/10.1039/C9ME00039A>.
41. Yang, K., Swanson, K., Jin, W., Coley, C., Eiden, P., Gao, H., Guzman-Perez, A., Hopper, T., Kelley, B., Mathea, M., et al. (2019). Analyzing Learned Molecular Representations for Property Prediction. Preprint at arXiv. <https://doi.org/10.48550/arXiv.1904.01561>.
42. Coley, C.W., Barzilay, R., Green, W.H., Jaakkola, T.S., and Jensen, K.F. (2017). Convolutional Embedding of Attributed Molecular Graphs for Physical Property Prediction. *J. Chem. Inf. Model.* *57*, 1757–1772. <https://doi.org/10.1021/acs.jcim.6b00601>.
43. Zhou, J., Cui, G., Zhang, Z., Yang, C., Liu, Z., Wang, L., Li, C., and Sun, M. (2019). Graph Neural Networks: A Review of Methods and Applications. Preprint at arXiv. <https://doi.org/10.48550/arXiv.1812.08434>.
44. Zitnik, M., Agrawal, M., and Leskovec, J. (2018). Modeling polypharmacy side effects with graph convolutional networks. *Bioinformatics* *34*, i457–i466. <https://doi.org/10.1093/bioinformatics/bty294>.
45. Coley, C.W., Jin, W., Rogers, L., Jamison, T.F., Jaakkola, T.S., Green, W.H., Barzilay, R., and Jensen, K.F. (2019). A graph-convolutional neural network model for the prediction of chemical reactivity. *Chem. Sci.* *10*, 370–377. <https://doi.org/10.1039/C8SC04228D>.
46. You, J., Liu, B., Ying, R., Pande, V., and Leskovec, J. 2018. Graph convolutional policy network for goal-directed molecular graph generation. In *Proceedings of the 32nd International Conference on Neural Information Processing Systems*, pp. 6412–6422.
47. McCall, I.C., Shah, N., Govindan, A., Baquero, F., and Levin, B.R. (2019). Antibiotic Killing of Diversely Generated Populations of Nonreplicating Bacteria. *Antimicrob. Agents Chemother.* *63*, e02360-18. <https://doi.org/10.1128/AAC.02360-18>.
48. Eun, Y.-J., Foss, M.H., Kiekebusch, D., Pauw, D.A., Westler, W.M., Thanbichler, M., and Weibel, D.B. (2012). DCAP: A Broad-Spectrum Antibiotic That Targets the Cytoplasmic Membrane of Bacteria. *J. Am. Chem. Soc.* *134*, 11322–11325. <https://doi.org/10.1021/ja302542j>.
49. Zhang, Y., Tangandanchu, V.K.R., Cheng, Y., Yang, R.-G., Lin, J.-M., and Zhou, C.-H. (2018). Potential Antimicrobial Isopropanol-Conjugated Carbazole Azoles as Dual Targeting Inhibitors of *Enterococcus faecalis*. *ACS Med. Chem. Lett.* *9*, 244–249. <https://doi.org/10.1021/acsmchemlett.7b00514>.
50. Lin, S., Liu, J., Li, H., Liu, Y., Chen, Y., Luo, J., and Liu, S. (2020). Development of Highly Potent Carbazole Amphiphiles as Membrane-Targeting Antimicrobials for Treating Gram-Positive Bacterial Infections. *J. Med. Chem.* *63*, 9284–9299. <https://doi.org/10.1021/acs.jmedchem.0c00433>.
51. Theodore, A., Lewis, K., and Vulić, M. (2013). Tolerance of *Escherichia coli* to Fluoroquinolone Antibiotics Depends on Specific Components of the SOS Response Pathway. *Genetics* *195*, 1265–1276. <https://doi.org/10.1534/genetics.113.152306>.
52. Usui, M., Yokoo, H., Tamura, Y., Nakajima, C., Suzuki, Y., Ghigo, J.-M., and Beloin, C. (2019). Zinc Acetate Potentiates the Action of Tosufloxacin against *Escherichia coli* Biofilm Persisters. *Antimicrob. Agents Chemother.* *63*, e00069-19. <https://doi.org/10.1128/AAC.00069-19>.
53. Greco, I., Molchanova, N., Holmedal, E., Jenssen, H., Hummel, B.D., Watts, J.L., Håkansson, J., Hansen, P.R., and Svenson, J. (2020). Correlation between hemolytic activity, cytotoxicity and systemic *in vivo* toxicity of synthetic antimicrobial peptides. *Sci. Rep.* *10*, 13206. <https://doi.org/10.1038/s41598-020-69995-9>.

54. Vattimo, M.d.F.F., Watanabe, M., da Fonseca, C.D., Neiva, L.B.d.M., Pessoa, E.A., and Borges, F.T. (2016). Polymyxin B Nephrotoxicity: From Organ to Cell Damage. *PLoS One* 11, e0161057. <https://doi.org/10.1371/journal.pone.0161057>.
55. Piorecka, K., Kurjata, J., and Stanczyk, W.A. (2022). Acriflavine, an Acridine Derivative for Biomedical Application: Current State of the Art. *J. Med. Chem.* 65, 11415–11432. <https://doi.org/10.1021/acs.jmedchem.2c00573>.
56. Chen, J., Ghorai, M.K., Kenney, G., and Stubbe, J. (2008). Mechanistic studies on bleomycin-mediated DNA damage: multiple binding modes can result in double-stranded DNA cleavage. *Nucleic Acids Res.* 36, 3781–3790. <https://doi.org/10.1093/nar/gkn302>.
57. Roy, S., Bahar, A.A., Gu, H., Nangia, S., Sauer, K., and Ren, D. (2021). Persistor control by leveraging dormancy associated reduction of antibiotic efflux. *PLoS Pathog.* 17, e1010144. <https://doi.org/10.1371/journal.ppat.1010144>.
58. Knudsen, G.M., Ng, Y., and Gram, L. (2013). Survival of Bactericidal Antibiotic Treatment by a Persister Subpopulation of *Listeria monocytogenes*. *Appl. Environ. Microbiol.* 79, 7390–7397. <https://doi.org/10.1128/AEM.02184-13>.
59. Wang, J., Grishin, A.V., and Ford, H.R. (2016). Experimental anti-inflammatory drug Semapimod inhibits Toll-like receptor signaling by targeting the TLR chaperone gp96. *J. Immunol.* 196, 5130–5137. <https://doi.org/10.4049/jimmunol.1502135>.
60. Sveinbjörnsson, B., Camilio, K.A., Haug, B.E., and Rekdal, Ø. (2017). LTX-315: a first-in-class oncolytic peptide that reprograms the tumor microenvironment. *Future Med. Chem.* 9, 1339–1344. <https://doi.org/10.4155/fmc-2017-0088>.
61. Spicer, J., Marabelle, A., Baurain, J.-F., Jebsen, N.L., Jøssang, D.E., Awada, A., Kristeleit, R., Loirat, D., Lazaridis, G., Jungels, C., et al. (2021). Safety, Antitumor Activity, and T-cell Responses in a Dose-Ranging Phase I Trial of the Oncolytic Peptide LTX-315 in Patients with Solid Tumors. *Clin. Cancer Res.* 27, 2755–2763. <https://doi.org/10.1158/1078-0432.CCR-20-3435>.
62. Bombrun, A., Gerber, P., Casi, G., Terradillos, O., Antonsson, B., and Halazy, S. (2003). 3,6-dibromocarbazole piperazine derivatives of 2-propanol as first inhibitors of cytochrome c release via Bax channel modulation. *J. Med. Chem.* 46, 4365–4368. <https://doi.org/10.1021/jm034107j>.
63. Dotan, I., Rachmilewitz, D., Schreiber, S., Eliakim, R., van der Woude, C.J., Kornbluth, A., Buchman, A.L., Bar-Meir, S., Bokemeyer, B., Goldin, E., et al. (2010). A randomised placebo-controlled multicentre trial of intravenous semapimod HCl for moderate to severe Crohn's disease. *Gut* 59, 760–766. <https://doi.org/10.1136/gut.2009.179994>.
64. Hommes, D., van den Blink, B., Plasse, T., Bartelsman, J., Xu, C., Macpherson, B., Tytgat, G., Peppelenbosch, M., and Van Deventer, S. (2002). Inhibition of stress-activated MAP kinases induces clinical improvement in moderate to severe Crohn's disease. *Gastroenterology* 122, 7–14. <https://doi.org/10.1053/gast.2002.30770>.
65. Atkins, M.B., Redman, B., Mier, J., Gollub, J., Weber, J., Sosman, J., MacPherson, B.L., and Plasse, T. (2001). A phase I study of CN1-1493, an inhibitor of cytokine release, in combination with high-dose interleukin-2 in patients with renal cancer and melanoma. *Clin. Cancer Res.* 7, 486–492.
66. Miller, I.S., Didier, S., Murray, D.W., Turner, T.H., Issaivanan, M., Ruggieri, R., Al-Abed, Y., and Symons, M. (2014). Semapimod Sensitizes Glioblastoma Tumors to Ionizing Radiation by Targeting Microglia. *PLoS One* 9, e95885. <https://doi.org/10.1371/journal.pone.0095885>.
67. Bevec, D., Hauber, J., Obert, S., Keri, G., Orfi, L., Szekely, I., Choidas, A., and Bacher, G. (2001). Pharmaceutically Active Aromatic Guanylylhydrazones.
68. Stokes, J.M., MacNair, C.R., Ilyas, B., French, S., Côté, J.P., Bouwman, C., Farha, M.A., Sieron, A.O., Whitfield, C., Coombes, B.K., and Brown, E.D. (2017). Pentamidine sensitizes Gram-negative pathogens to antibiotics and overcomes acquired colistin resistance. *Nat. Microbiol.* 2, 17028. <https://doi.org/10.1038/nmicrobiol.2017.28>.
69. Nikaido, H., and Vaara, M. (1985). Molecular basis of bacterial outer membrane permeability. *Microbiol. Rev.* 49, 1–32. <https://doi.org/10.1128/mr.49.1.1-32.1985>.
70. Vaara, M. (1993). Outer membrane permeability barrier to azithromycin, clarithromycin, and roxithromycin in gram-negative enteric bacteria. *Antimicrob. Agents Chemother.* 37, 354–356.
71. Tuson, H.H., Auer, G.K., Renner, L.D., Hasebe, M., Tropini, C., Salick, M., Crone, W.C., Gopinathan, A., Huang, K.C., and Weibel, D.B. (2012). Measuring the stiffness of bacterial cells from growth rates in hydrogels of tunable elasticity: Measuring cellular mechanical properties with hydrogels. *Mol. Microbiol.* 84, 874–891. <https://doi.org/10.1111/j.1365-2958.2012.08063.x>.
72. Li, A., Schertzer, J.W., and Yong, X. (2018). Molecular Dynamics Modeling of *Pseudomonas Aeruginosa* Outer Membranes. *Phys. Chem. Chem. Phys.* 20, 23635–23648. <https://doi.org/10.1039/c8cp04278k>.
73. Yoshimura, F., and Nikaido, H. (1982). Permeability of *Pseudomonas aeruginosa* outer membrane to hydrophilic solutes. *J. Bacteriol.* 152, 636–642.
74. Nikaido, H. (2003). Molecular basis of bacterial outer membrane permeability revisited. *Microbiol. Mol. Biol. Rev.* 67, 593–656. <https://doi.org/10.1128/MMBR.67.4.593-656.2003>.
75. Manioglou, S., Modaresi, S.M., Ritzmann, N., Thoma, J., Overall, S.A., Harms, A., Upert, G., Luther, A., Barnes, A.B., Obrecht, D., et al. (2022). Antibiotic polymyxin arranges lipopolysaccharide into crystalline structures to solidify the bacterial membrane. *Nat. Commun.* 13, 6195. <https://doi.org/10.1038/s41467-022-33838-0>.
76. Wong, F., Stokes, J.M., Cervantes, B., Penkov, S., Friedrichs, J., Renner, L.D., and Collins, J.J. (2021). Cytoplasmic condensation induced by membrane damage is associated with antibiotic lethality. *Nat. Commun.* 12, 2321. <https://doi.org/10.1038/s41467-021-22485-6>.
77. Mood, E.H., Goltermann, L., Brolin, C., Cavaco, L.M., Nejad, A.J., Yavari, N., Frederiksen, N., Franzky, H., and Nielsen, P.E. (2021). Antibiotic Potentiation in Multidrug-Resistant Gram-Negative Pathogenic Bacteria by a Synthetic Peptidomimetic. *ACS Infect. Dis.* 7, 2152–2163. <https://doi.org/10.1021/acscinfecdis.1c00147>.
78. Velkov, T., Gallardo-Godoy, A., Swarbrick, J.D., Blaskovich, M.A.T., Elliott, A.G., Han, M., Thompson, P.E., Roberts, K.D., Huang, J.X., Becker, B., et al. (2018). Structure, Function, and Biosynthetic Origin of Octapeptide Antibiotics Active against Extensively Drug-Resistant Gram-Negative Bacteria. *Cell Chem. Biol.* 25, 380–391.e5. <https://doi.org/10.1016/j.chembiol.2018.01.005>.
79. Khadka, N.K., Aryal, C.M., and Pan, J. (2018). Lipopolysaccharide-Dependent Membrane Permeation and Lipid Clustering Caused by Cyclic Lipopeptide Colistin. *ACS Omega* 3, 17828–17834. <https://doi.org/10.1021/acsomega.8b02260>.
80. Olaitan, A.O., Morand, S., and Rolain, J.-M. (2014). Mechanisms of polymyxin resistance: acquired and intrinsic resistance in bacteria. *Front. Microbiol.* 5, 643.
81. Huang, J., Li, C., Song, J., Velkov, T., Wang, L., Zhu, Y., and Li, J. (2020). Regulating polymyxin resistance in Gram-negative bacteria: roles of two-component systems PhoPQ and PmrAB. *Future Microbiol.* 15, 445–459. <https://doi.org/10.2217/fmb-2019-0322>.
82. MacNair, C.R., Stokes, J.M., Carrae, L.A., Fiebig-Comyn, A.A., Coombes, B.K., Mulvey, M.R., and Brown, E.D. (2018). Overcoming mcr-1 mediated colistin resistance with colistin in combination with other antibiotics. *Nat. Commun.* 9, 458. <https://doi.org/10.1038/s41467-018-02875-z>.
83. Brennan-Krohn, T., Pironti, A., and Kirby, J.E. (2018). Synergistic Activity of Colistin-Containing Combinations against Colistin-Resistant Enterobacteriaceae. *Antimicrob. Agents Chemother.* 62, e00873-18. <https://doi.org/10.1128/AAC.00873-18>.

84. Sabnis, A., Hagart, K.L., Klöckner, A., Becce, M., Evans, L.E., Furniss, R.C.D., Mavridou, D.A., Murphy, R., Stevens, M.M., Davies, J.C., et al. (2021). Colistin kills bacteria by targeting lipopolysaccharide in the cytoplasmic membrane. *Elife* 10, e65836. <https://doi.org/10.7554/eLife.65836>.
85. Christensen, D.G., Orr, J.S., Rao, C.V., and Wolfe, A.J. (2017). Increasing Growth Yield and Decreasing Acetylation in *Escherichia coli* by Optimizing the Carbon-to-Magnesium Ratio in Peptide-Based Media. *Appl. Environ. Microbiol.* 83, e03034-16. <https://doi.org/10.1128/AEM.03034-16>.
86. Workinger, J.L., Doyle, R.P., and Bortz, J. (2018). Challenges in the Diagnosis of Magnesium Status. *Nutrients* 10, 1202. <https://doi.org/10.3390/nu10091202>.
87. Nikaido, H., and Hancock, R.E.W. (1986). Outer Membrane Permeability of *Pseudomonas aeruginosa*. In *The Biology of Pseudomonas* (Elsevier), pp. 145–193. <https://doi.org/10.1016/B978-0-12-307210-8.50009-9>.
88. Bystrova, O.V., Shashkov, A.S., Kocharova, N.A., Knirel, Y.A., Lindner, B., Zähringer, U., and Pier, G.B. (2002). Structural studies on the core and the O-polysaccharide repeating unit of *Pseudomonas aeruginosa* immunotype 1 lipopolysaccharide. *Eur. J. Biochem.* 269, 2194–2203. <https://doi.org/10.1046/j.1432-1033.2002.02875.x>.
89. El-Sayed Ahmed, M.A.E.-G., Zhong, L.-L., Shen, C., Yang, Y., Doi, Y., and Tian, G.-B. (2020). Colistin and its role in the Era of antibiotic resistance: an extended review (2000–2019). *Emerg. Microb. Infect.* 9, 868–885. <https://doi.org/10.1080/22221751.2020.1754133>.
90. Savitski, M.M., Reinhard, F.B.M., Franken, H., Werner, T., Savitski, M.F., Eberhard, D., Martinez Molina, D., Jafari, R., Dovega, R.B., Klaeger, S., et al. (2014). Tracking cancer drugs in living cells by thermal profiling of the proteome. *Science* 346, 1255784. <https://doi.org/10.1126/science.1255784>.
91. Franken, H., Mathieson, T., Childs, D., Sweetman, G.M.A., Werner, T., Tögel, I., Doce, C., Gade, S., Bantscheff, M., Drewes, G., et al. (2015). Thermal proteome profiling for unbiased identification of direct and indirect drug targets using multiplexed quantitative mass spectrometry. *Nat. Protoc.* 10, 1567–1593. <https://doi.org/10.1038/nprot.2015.101>.
92. Herneisen, A.L., Li, Z.-H., Chan, A.W., Moreno, S.N.J., and Lourido, S. (2022). Temporal and thermal profiling of the *Toxoplasma* proteome implicates parasite Protein Phosphatase 1 in the regulation of Ca<sup>2+</sup>-responsive pathways. *Elife* 11, e80336. <https://doi.org/10.7554/eLife.80336>.
93. Brown, E.D., and Wright, G.D. (2016). Antibacterial drug discovery in the resistance era. *Nature* 529, 336–343. <https://doi.org/10.1038/nature17042>.
94. Radlinski, L., and Conlon, B.P. (2018). Antibiotic efficacy in the complex infection environment. *Curr. Opin. Microbiol.* 42, 19–24. <https://doi.org/10.1016/j.mib.2017.09.007>.
95. Goldman, B., Kearnes, S., Kramer, T., Riley, P., and Walters, W.P. (2022). Defining Levels of Automated Chemical Design. *J. Med. Chem.* 65, 7073–7087. <https://doi.org/10.1021/acs.jmedchem.2c00334>.
96. Wong, F., de la Fuente-Nunez, C., and Collins, J.J. (2023). Leveraging artificial intelligence in the fight against infectious diseases. *Science* 381, 164–170.
97. (2015). New Indications and a Sense of (Re)purpose. *EBioMedicine* 2, 1257–1258. <https://doi.org/10.1016/j.ebiom.2015.10.003>.
98. Coley, C.W., Eyke, N.S., and Jensen, K.F. (2020). Autonomous Discovery in the Chemical Sciences Part II: Outlook. *Angew. Chem., Int. Ed. Engl.* 59, 23414–23436. <https://doi.org/10.1002/anie.201909989>.
99. Sorlí, L., Luque, S., Grau, S., Berenguer, N., Segura, C., Montero, M.M., Alvarez-Lerma, F., Knobel, H., Benito, N., and Horcajada, J.P. (2013). Trough colistin plasma level is an independent risk factor for nephrotoxicity: a prospective observational cohort study. *BMC Infect. Dis.* 13, 380. <https://doi.org/10.1186/1471-2334-13-380>.
100. Eckert, R. (2011). Road to clinical efficacy: challenges and novel strategies for antimicrobial peptide development. *Future Microbiol.* 6, 635–651. <https://doi.org/10.2217/fmb.11.27>.
101. Herzog, I.M., and Fridman, M. (2014). Design and synthesis of membrane-targeting antibiotics: from peptides- to aminosugar-based antimicrobial cationic amphiphiles. *Med. Chem. Commun.* 5, 1014–1026. <https://doi.org/10.1039/C4MD00012A>.
102. Falagas, M.E., and Kasiakou, S.K. (2005). Colistin: the revival of polymyxins for the management of multidrug-resistant gram-negative bacterial infections. *Clin. Infect. Dis.* 40, 1333–1341. <https://doi.org/10.1086/429323>.
103. Huisman, G.W., Siegele, D.A., and Zambrano, M.M. (1996). Morphological and physiological changes during stationary phase. In *Escherichia coli and Salmonella: cellular and molecular biology*, F.C. Neidhardt, et al., eds. (Washington, D.C: ASM Press), pp. 1672–1682.
104. Navarro Llorens, J.M., Tormo, A., and Martínez-García, E. (2010). Stationary phase in gram-negative bacteria. *FEMS Microbiol. Rev.* 34, 476–495. <https://doi.org/10.1111/j.1574-6976.2010.00213.x>.
105. Delcour, A.H. (2009). Outer Membrane Permeability and Antibiotic Resistance. *Biochim. Biophys. Acta* 1794, 808–816. <https://doi.org/10.1016/j.bbapap.2008.11.005>.
106. Silver, L.L. (2011). Challenges of Antibacterial Discovery. *Clin. Microbiol. Rev.* 24, 71–109. <https://doi.org/10.1128/cmr.00030-10>.
107. Wong, F., Wilson, S., Helbig, R., Hegde, S., Aftenieva, O., Zheng, H., Liu, C., Pilizota, T., Garner, E.C., Amir, A., and Renner, L.D. (2021). Understanding Beta-Lactam-Induced Lysis at the Single-Cell Level. *Front. Microbiol.* 12, 712007. <https://doi.org/10.3389/fmicb.2021.712007>.
108. Nau, R., and Eiffert, H. (2005). Minimizing the release of proinflammatory and toxic bacterial products within the host: A promising approach to improve outcome in life-threatening infections. *FEMS Immunol. Med. Microbiol.* 44, 1–16. <https://doi.org/10.1016/j.femsim.2005.01.001>.
109. Coates, A., Hu, Y., Bax, R., and Page, C. (2002). The future challenges facing the development of new antimicrobial drugs. *Nat. Rev. Drug Discov.* 1, 895–910. <https://doi.org/10.1038/nrd940>.
110. Van den Bergh, B., Michiels, J.E., Fauvart, M., and Michiels, J. (2016). Should we develop screens for multi-drug antibiotic tolerance? *Expert Rev. Anti Infect. Ther.* 14, 613–616. <https://doi.org/10.1080/14787210.2016.1194754>.
111. Landrum G. RDKit. <https://doi.org/10.5281/zenodo.3732262>.
112. Wong, F., Omori, S., Donghia, N.M., Zheng, E.J., and Collins, J.J. (2023). Discovering small-molecule senolytics with deep neural networks. *Nat Aging* 3, 734–750.
113. Clemons, P.A., Bittker, J.A., Wagner, F.F., Hands, A., Dančik, V., Schreiber, S.L., Choudhary, A., and Wagner, B.K. (2021). The Use of Informer Sets in Screening: Perspectives on an Efficient Strategy to Identify New Probes. *SLAS Discov.* 26, 855–861. <https://doi.org/10.1177/24725552211019410>.
114. Mendez, D., Gaulton, A., Bento, A.P., Chambers, J., De Veij, M., Félix, E., Magariños, M.P., Mosquera, J.F., Mutowo, P., Nowotka, M., et al. (2019). ChEMBL: towards direct deposition of bioassay data. *Nucleic Acids Res.* 47, D930–D940. <https://doi.org/10.1093/nar/gky1075>.
115. Pedregosa, F., Varoquaux, G., Gramfort, A., Michel, V., Thirion, B., Grisel, O., Blondel, M., Prettenhofer, P., Weiss, R., Dubourg, V., et al. (2011). Scikit-learn: Machine Learning in Python. *J. Mach. Learn. Res.* 12, 2825–2830.
116. Sievert, C (2020). Interactive Web-Based Data Visualization with R, plotly, and shiny. Chapman and Hall/CRC. <https://plotly-r.com>.
117. Müller, A., Wenzel, M., Strahl, H., Grein, F., Saaki, T.N.V., Kohl, B., Siersma, T., Bandow, J.E., Sahl, H.-G., Schneider, T., and Hamoen, L.W. (2016). Daptomycin inhibits cell envelope synthesis by interfering with fluid membrane microdomains. *Proc. Natl. Acad. Sci. USA* 113, E7077–E7086. <https://doi.org/10.1073/pnas.1611173113>.

118. Ipsen, J.Ø., and Sørensen, D.M. (2022). ATP hydrolytic activity of purified Spf1p correlate with micellar lipid fluidity and is dependent on conserved residues in transmembrane helix M1. *PLoS One* *17*, e0274908. <https://doi.org/10.1371/journal.pone.0274908>.
119. Ducret, A., Quardokus, E.M., and Brun, Y.V. (2016). MicrobeJ, a tool for high throughput bacterial cell detection and quantitative analysis. *Nat. Microbiol.* *1*, 16077. <https://doi.org/10.1038/nmicrobiol.2016.77>.
120. Schindelin, J., Arganda-Carreras, I., Frise, E., Kaynig, V., Longair, M., Pietzsch, T., Preibisch, S., Rueden, C., Saalfeld, S., Schmid, B., et al. (2012). Fiji: an open-source platform for biological-image analysis. *Nat. Methods* *9*, 676–682. <https://doi.org/10.1038/nmeth.2019>.
121. Kim, W., Zhu, W., Hendricks, G.L., Van Tyne, D., Steele, A.D., Keohane, C.E., Fricke, N., Conery, A.L., Shen, S., Pan, W., et al. (2018). A new class of synthetic retinoid antibiotics effective against bacterial persisters. *Nature* *556*, 103–107. <https://doi.org/10.1038/nature26157>.
122. Li, H., and Durbin, R. (2009). Fast and accurate short read alignment with Burrows-Wheeler transform. *Bioinformatics* *25*, 1754–1760. <https://doi.org/10.1093/bioinformatics/btp324>.
123. Walker, B.J., Abeel, T., Shea, T., Priest, M., Abouelliel, A., Sakthikumar, S., Cuomo, C.A., Zeng, Q., Wortman, J., Young, S.K., and Earl, A.M. (2014). Pilon: An Integrated Tool for Comprehensive Microbial Variant Detection and Genome Assembly Improvement. *PLoS One* *9*, e112963. <https://doi.org/10.1371/journal.pone.0112963>.
124. Hughes, C.S., Moggridge, S., Müller, T., Sorensen, P.H., Morin, G.B., and Krijgsveld, J. (2019). Single-pot, solid-phase-enhanced sample preparation for proteomics experiments. *Nat. Protoc.* *14*, 68–85. <https://doi.org/10.1038/s41596-018-0082-x>.
125. Bekker-Jensen, D.B., Martínez-Val, A., Steigerwald, S., Rütther, P., Fort, K.L., Arrey, T.N., Harder, A., Makarov, A., and Olsen, J.V. (2020). A Compact Quadrupole-Orbitrap Mass Spectrometer with FAIMS Interface Improves Proteome Coverage in Short LC Gradients. *Mol. Cell. Proteomics* *19*, 716–729. <https://doi.org/10.1074/mcp.TIR119.001906>.
126. Perez-Riverol, Y., Bai, J., Bandla, C., García-Seisdedos, D., Hewapathirana, S., Kamatchinathan, S., Kundu, D.J., Prakash, A., Frericks-Zipper, A., Eisenacher, M., et al. (2022). The PRIDE database resources in 2022: a hub for mass spectrometry-based proteomics evidences. *Nucleic Acids Res.* *50*, D543–D552. <https://doi.org/10.1093/nar/gkab1038>.
127. R Core Team (2020). European Environment Agency. <https://www.eea.europa.eu/data-and-maps/indicators/oxygen-consuming-substances-in-rivers/r-development-core-team-2006>.
128. Cox, J., and Mann, M. (2008). MaxQuant enables high peptide identification rates, individualized p.p.b.-range mass accuracies and proteome-wide protein quantification. *Nat. Biotechnol.* *26*, 1367–1372. <https://doi.org/10.1038/nbt.1511>.
129. Kitagawa, M., Ara, T., Arifuzzaman, M., Ioka-Nakamichi, T., Inamoto, E., Toyonaga, H., and Mori, H. (2005). Complete set of ORF clones of *Escherichia coli* ASKA library (a complete set of *E. coli* K-12 ORF archive): unique resources for biological research. *DNA Res.* *12*, 291–299. <https://doi.org/10.1093/dnares/dsi012>.
130. Baba, T., Ara, T., Hasegawa, M., Takai, Y., Okumura, Y., Baba, M., Datsenko, K.A., Tomita, M., Wanner, B.L., and Mori, H. (2006). Construction of *Escherichia coli* K-12 in-frame, single-gene knockout mutants: the Keio collection. *Mol. Syst. Biol.* *2*, 2006.0008. <https://doi.org/10.1038/msb4100050>.

STAR★METHODS

KEY RESOURCES TABLE

REAGENT or RESOURCE	SOURCE	IDENTIFIER
<b>Bacterial and virus strains</b>		
<i>E. coli</i> BW25113	CGSC	Cat# 7636
<i>E. coli</i> ATCC 25922	ATCC	Cat# 25922
<i>E. coli</i> K-12 MG1655	ATCC	Cat# 700926
<i>E. coli</i> W3110	CGSC	Cat# 4474
<i>P. aeruginosa</i> PAO1	ATCC	Cat# 47085
<i>K. pneumoniae</i> ATCC 13883	ATCC	Cat# 13883
<i>A. baumannii</i> ATCC 17978	ATCC	Cat# 17978
<b>Chemicals, peptides, and recombinant proteins</b>		
Semapimod hydrochloride	BOC Sciences	Cat# B2693-462782
Drug Repurposing Hub	Broad Institute	<a href="https://repo-hub.broadinstitute.org/repurposing">https://repo-hub.broadinstitute.org/repurposing</a>
Broad Institute 800K Compound Database	Broad Institute	<a href="https://github.com/jackievaleri/nontoxic_stat_phase_killing_abx">https://github.com/jackievaleri/nontoxic_stat_phase_killing_abx</a>
1-N-phenyl-naphthylamine (NPN)	Sigma-Aldrich	Cat# 104043
<i>E. coli</i> LPS	Sigma-Aldrich	Cat# L3129
<i>K. pneumoniae</i> LPS	Sigma-Aldrich	Cat# L4268
<i>P. aeruginosa</i> LPS	Sigma-Aldrich	Cat# L9143
BODIPY-cadaverine	Molecular Probes	Cat# D6251
LAL reagent	Thermo Scientific	Cat# 88282
250 U/μl benzonase	Sigma-Aldrich	Cat# E1014-25KU
100× Halt Protease Inhibitor Cocktail	Life Technologies	Cat# 87786
IGEPAL® CA-630 viscous liquid (NP-40)	Sigma-Aldrich	Cat# I3021-50ML
DC Protein Assay	Bio-Rad	Cat# 5000116
Tris(2-carboxyethyl)phosphine (TCEP)	Pierce	Cat# 20490
Methyl methanethiosulfonate (MMTS)	Thermo Fisher Scientific	Cat# 23011
Ethyl alcohol, Pure 200 proof, HPLC grade	Sigma-Aldrich	Cat# 459828-1L
Triethylammonium bicarbonate buffer 1M (TEAB)	Sigma-Aldrich	Cat# T7408-100ML
Pierce Quantitative Fluorometric Peptide Assay	Thermo Fisher Scientific	Cat# 23290
TMT10plex Isobaric Label Reagent Set	Thermo Fisher Scientific	Cat# 90110
50% hydroxylamine	Thermo Fisher Scientific	Cat# 90115
Pierce high pH fractionation kit	Thermo Fisher Scientific	Cat# 84868
Ultra-high-performance liquid chromatography (UPLC)-MS acetonitrile	Thermo Fisher Scientific	Cat# A9561
<b>Deposited data</b>		
DNA sequencing of semapimod evolution	This study – deposited in SRA	PRJNA1010194
Thermal proteome profiling	This study – deposited in PRIDE	<a href="https://doi.org/10.6019/PXD044230">https://doi.org/10.6019/PXD044230</a>
Raw and analyzed data	This paper	<a href="https://github.com/jackievaleri/nontoxic_stat_phase_killing_abx">https://github.com/jackievaleri/nontoxic_stat_phase_killing_abx</a>
<b>Experimental models: Cell lines</b>		
HepG2	ATCC	Cat# HB-8065
HEK-293	ATCC	Cat# CRL-1573
Rat Sprague Dawley Red Blood Cells	Innovative Research	Cat# IRTSDRBC
<b>Recombinant DNA</b>		
pGDP2-mcr-1 plasmid	Addgene	pGDP2 MCR-1 was a gift from Gerard Wright (Addgene plasmid #118404)

(Continued on next page)

**Continued**

REAGENT or RESOURCE	SOURCE	IDENTIFIER
Software and algorithms		
Prism 9	Graphpad	<a href="http://www.graphpad.com/scientific-software/prism/">www.graphpad.com/scientific-software/prism/</a>
Original code	This paper	<a href="https://github.com/jackievaleri/nontoxic_stat_phase_killing_abx">https://github.com/jackievaleri/nontoxic_stat_phase_killing_abx</a> and <a href="https://doi.org/10.5281/zenodo.8401264">https://doi.org/10.5281/zenodo.8401264</a>
Chemprop	Yang et al., 2019 <sup>41</sup>	<a href="https://github.com/chemprop/chemprop">https://github.com/chemprop/chemprop</a>
RDKit	Landrum, 2010 <sup>111</sup>	<a href="https://www.rdkit.org">https://www.rdkit.org</a>
Plotly Express	Sievert, 2020 <sup>116</sup>	<a href="https://plotly-r.com">https://plotly-r.com</a>
Scikit-Learn	Pedregosa et al., 2011 <sup>115</sup>	<a href="https://scikit-learn.org/stable/">https://scikit-learn.org/stable/</a>
Bcl-convert	Illumina	<a href="http://support.illumina.com/sequencing/sequencing_software/bcl-convert.html">support.illumina.com/sequencing/sequencing_software/bcl-convert.html</a>
Burrows-Wheeler transform	Li and Durbin, 2009 <sup>122</sup>	<a href="https://github.com/lh3/bwa">github.com/lh3/bwa</a>
Pilon	Walker et al., 2014 <sup>123</sup>	<a href="https://software.broadinstitute.org/software/pilon/">https://software.broadinstitute.org/software/pilon/</a>
HISAT2		<a href="http://daehwankimlab.github.io/hisat2/">http://daehwankimlab.github.io/hisat2/</a>
featureCounts		<a href="https://www.rdocumentation.org/packages/Rsubread/versions/1.22.2/topics/featureCounts">https://www.rdocumentation.org/packages/Rsubread/versions/1.22.2/topics/featureCounts</a>
edgeR		<a href="https://bioconductor.org/packages/release/bioc/html/edgeR.html">https://bioconductor.org/packages/release/bioc/html/edgeR.html</a>
MicrobeJ	Ducret et al., 2016 <sup>119</sup>	<a href="https://www.microbej.com/download-2/">https://www.microbej.com/download-2/</a>
Fiji	Schindelin et al., 2012 <sup>120</sup>	<a href="https://imagej.net/software/fiji/">https://imagej.net/software/fiji/</a>
TPP	Franken et al., 2015 <sup>91</sup>	<a href="https://www.bioconductor.org/packages/release/bioc/html/TPP.html">https://www.bioconductor.org/packages/release/bioc/html/TPP.html</a>

**RESOURCE AVAILABILITY****Lead contact**

Further information and requests for resources and reagents should be directed to James J. Collins ([jimjc@mit.edu](mailto:jimjc@mit.edu)).

**Materials availability**

This study did not generate new unique reagents.

**Data and code availability**

- Sequencing data have been deposited at the Sequence Read Archive repository and are publicly available as of the date of publication. Thermal proteome profiling data have been deposited at PRIDE and are publicly available as of the date of publication. Raw data have been deposited at Github and Zenodo and are publicly available as of the date of submission. Accession numbers are listed in the [key resources table](#).
- All original code and computational analyses have been deposited at Github and Zenodo and is publicly available as of the date of submission. DOIs are listed in the [key resources table](#).
- Any additional information required to reanalyze the data reported in this paper is available from the [lead contact](#) upon request.

**EXPERIMENTAL MODEL AND STUDY PARTICIPANT DETAILS**

Experiments were conducted at 37°C unless otherwise noted. HEK-293 CRL-1573 (ATCC) is a female cell line and HEPG2 HB-8065 (ATCC) is a male cell line. All information on alternate temperature conditions, strains, as well as media conditions for experiments, can be found in the [method details](#) section.

**METHOD DETAILS****Dilution-regrowth screen to assess stationary-phase lethality**

An overnight culture of *E. coli* BW25113 (Ec BW) was grown in LB broth, then diluted 1:10,000 into 50 mL of 1% LB in PBS and grown in 250 mL non-baffled flasks for 24 hours at 37°C, 300 rpm shaking. After 24 hours, 40 µL of culture was added to each well of 384-well Drug Repurposing Hub plates for a final screening concentration of 50 µM, and plates were incubated in sealed plastic bags at 37°C

for 24 hours. Following this, an Agilent Bravo robot was used to transfer 1  $\mu\text{L}$  of treated culture into 200  $\mu\text{L}$  of LB broth in 96-well plates. These plates were incubated in sealed plastic bags at 37°C for 24 hours, then OD<sub>600</sub> readings were taken on a Spectramax M3 plate reader (Molecular Devices). Data were normalized based on the inter-quartile mean of the plate, and compounds that had a normalized OD<sub>600</sub> of <0.2 in either replicate were validated in the colony forming unit assay as described below.

### Stationary-phase killing colony forming unit determination

An overnight culture of Ec BW grown in LB broth was diluted 1:10,000 into 50 mL of 1% LB broth in PBS in non-baffled 250 mL flasks. Cells were grown for 24 hours at 37°C, 300 rpm shaking, then distributed in a 96-well plate with compound for a total volume of 100  $\mu\text{L}$ . Plates were then incubated for another 24 hours at 37°C, 900 rpm shaking, then washed twice with PBS. Finally, samples were serially diluted 10-fold in PBS and 7  $\mu\text{L}$  was spotted on LB agar plates to quantify CFU. For CFU validation of the dilution-re-growth screen, compounds that killed greater than a log of bacteria (from the DMSO-treated control) across two replicates were marked as active.

### Growth inhibition screen

An overnight culture of Ec BW was diluted 1 in 10,000 in LB broth, and 40  $\mu\text{L}$  was added to each well of 384-well Drug Repurposing Hub plates for a screening concentration of 50  $\mu\text{M}$ . Plates were placed in sealed plastic bags, incubated at 37°C for 24 hours, and then OD<sub>600</sub> was read. Plates were normalized by inter-quartile mean, and compounds were marked as active if both replicates had a normalized OD<sub>600</sub> of <0.2, and as non-active if either or both replicates had a normalized OD<sub>600</sub> of >0.2.

### Growth inhibitory model on new screening data

A graph neural network was trained using the Chemprop package to evaluate the ability of existing data and models to predict the killing activity screening data. Architecture and hyperparameters were obtained from Stokes et al., 2020:<sup>23</sup> the model was initialized with a dropout of 0.35, hidden size of 1600, 1 FFN layer, and depth of 5 with 2-dimensional normalized RDKit features and all other defaults. Table S1B from Stokes et al., 2020<sup>23</sup> was used to train the model for growth inhibitory activity predictions. The final model was tested on the new DRH screening data after removing any identical compounds from the DRH with the same structure as compounds in Table S1B.

### Data pre-processing for model training

Datasets from stationary-phase killing and growth inhibition screens were split into an 80% training set and 20% testing set. The training and test sets were class-balanced with regard to active compounds (for the purposes of splitting the data, a compound was considered active if it had either growth inhibitory and/or killing activity), with equal proportions of active compounds in the training set and the testing set. For each training and test set compound, 200 global biophysical features (molecular weight, beta-lactam fragment presence, logP, etc.) were computed via RDKit<sup>111</sup> using the Descriptastorus package (<https://github.com/bp-kelley/descriptastorus>).

### Model architecture and training

A graph neural network (GNN) was trained with the 80% train set using the Chemprop package as in Stokes et al., 2020.<sup>23</sup> In brief, the model consists of several graph convolutional layers that aggregate local ‘neighborhoods’ of molecular information into an embedding of arbitrary size by averaging the features associated with each bond. This embedding is then concatenated to the vector of Descriptastorus-generated features, and the modified embedding is passed to some number of feedforward layers before outputting a value between 0 and 1. This value can be interpreted as the antibacterial ‘score’ for each molecule, where the closer this value is to 1, the more likely it is for the compound to be antibacterial, and vice versa. All models are constructed with ReLU activation after every layer. The last layer has a sigmoid activation applied. The message-passing operation (i.e., the graph convolutional operation) is centered on bonds as nodes and atoms as edges in the molecular graph.

Here, the graph neural network was given the SMILES strings of the compounds as input data and both the inhibitory and killing binary scores as target values to predict. A hyperparameter optimization grid search was computed over the following parameters: dropout of 0.1, 0.25, and 0.4; number of feedforward layers 1 and 2; number of message-passing layers of 3, 4, and 5; initial learning rate of 0.001 and 0.0001; and number of nodes in each feedforward layer of 300, 500, 1,000, and 1,500. All models are trained for 30 epochs with a learning rate schedule as follows: the learning rate increases linearly for two ‘warm-up’ epochs between the initial learning rate and the maximum learning rate of 0.001, and then decreases exponentially from the maximum learning rate of 0.001 to the final learning rate of 0.0001. Models may stop earlier than the full number of epochs if the validation auROC has not improved according to an early stopping regime. Each architecture was trained with an 80% training / 10% validation / 10% testing split. The hyperparameter search was only performed on the 80% train set, such that the training data for any fold was 64% of the full dataset size; the 20% test set was completely held-out until after the search concluded. Models were evaluated over three folds generated with a scaffold-balanced splitting method: Murcko scaffolds of compounds were grouped by similarity and the largest scaffold classes were isolated into either the training or the test set for a more ‘real-world’-approximating evaluation of model performance.

Grid search models were assessed based on their performance on the 10% testing set. The model with best performance had the following architecture: dropout rate of 0.1, two feedforward layers, four message-passing layers, initial learning rate of 0.001, and 1,000 nodes in each feedforward layer. This model was predictive on the 10% test set, with a mean auROC of 0.898 predicting growth

inhibition and a mean auROC of 0.844 predicting stationary-phase killing. Next, this model was evaluated on the 20% held-out test set, maintaining its high performance with an auROC of 0.850 and auPR of 0.505 on growth inhibition prediction and a modest auROC of 0.740 and auPR of 0.055 on stationary-phase killing prediction, though we note there are only 11 positive compounds in the test set for the latter category. Finally, we trained 30 ensemble models with 100% of the available training data with this architecture, according to the same training protocol described earlier. This final ensemble model had an growth inhibition prediction auROC of 0.885 +/- 0.068 and a stationary-phase killing prediction auROC of 0.861 +/- 0.080 over 30 folds. For model training and deployment, a Google Cloud Platform virtual machine was used to run Ubuntu 18.04 with a 1 x NVIDIA Tesla K80 GPU, 8 vCPU, RAM 53248 MiB, and 500GB of storage.

### Shallow model comparison

To benchmark the more complex GNN against simpler, shallower models, the Chemprop package was used to test three types of models using Morgan fingerprints as input. First, a random forest classifier was tested, with a hyperparameter grid search conducted over the following parameters: number of bits in fingerprint: 512, 1,024, 2,048, and 4,096; radius of fingerprint: 2, 3, and 4; number of trees in the forest: 50, 100, 250, 500, 750, 1,000, and 2,000. The top-performing random forest classifier was a classifier with 2,000 trees trained on fingerprints with radius of 3 and 4,096 bits, achieving mean auROC of 0.810 on growth inhibition tasks and 0.723 on stationary-phase killing tasks. The support vector machines were optimized over the same number of bits and radius ranges. One SVM was trained for growth inhibition prediction alone and another trained for stationary-phase killing prediction alone, with the top growth inhibition model taking fingerprints of radius 2 and of length 4,096 bits, and achieving an auROC of 0.820. The top killing model takes fingerprints of radius 3 and of length 4,096 bits and achieves an auROC of 0.753. For both the RFC and SVM, 200 global RDKit features were added to the fingerprint vector as in the GNN. Lastly, an FFN was trained using binary Morgan fingerprints of radius 2 with 2,048 bits, and optimized over the following parameters: number of fully connected layers: 1, 2, 3, and 4; size of each layer: 500, 1,000, and 1,500; and dropout rate: 0.1, 0.2, and 0.3. The top FFN had three fully connected layers of 1,500 nodes each with a dropout rate of 0.3, and achieved an auROC of 0.715 on growth inhibition tasks and an auROC of 0.659 on killing tasks.

### Model deployment

We virtually screened a large chemical library by deploying the GNN on the Broad 800K library to predict growth inhibition and stationary-phase killing activity values.<sup>112</sup> This library is maintained by the Broad Institute's Center for the Development of Therapeutics and is composed of a variety of chemical sources, including the Drug Repurposing Hub, other known bioactives, external chemical vendor screening libraries, and compounds generated by diversity-oriented synthesis.<sup>113</sup> Out of the ~800,000 molecules, we carried forward only those that had predicted killing scores greater than 0.2 and <1 Tanimoto similarity to the training set, leaving 375 molecules. Tanimoto similarity was computed on 2,048-bit RDKit fingerprints. We further filtered for molecules with less than 0.9 Tanimoto similarity to the training set as well as less than 0.9 Tanimoto similarity to a set of known antibiotics as annotated on ChEMBL.<sup>114</sup> Note that for all subsequent analyses regarding antibiotics, we used a further refined, more curated dataset of antibacterial antibiotics that includes antiseptics.

### Antibiotic compound curation

Initial filtering to known antibiotics for machine learning compound curation used all compounds marked as 'antibiotic' on ChEMBL. This loosely defined set of compounds marked as 'antibiotic' on ChEMBL includes many known antibacterials and a few anti-cancer and anti-viral antibiotics. For future filtering steps such as those used to curate compounds in Figure 2E, a more stringent set of labelled antibiotic compounds (N=566) were obtained via the following steps: identifying compounds matching the keyword 'antibiotics' on ChEMBL; annotating all known classes or mechanisms of action; filtering out any anti-viral, anti-fungal, or anti-cancer antibiotics; adding in manually-selected classes without sufficient representation, such as nitrofurans, polymyxins, and antiseptics; and adding any missing drugs from the FDA-approved antibiotics list. These steps resulted in the following classes represented, in order from most compounds to least compounds per class: macrolide, glycopeptide, beta-lactam, tetracycline, aminoglycoside, anti-septic/membrane active, fluoroquinolone/quinolone, polymyxin, nitroimidazole, oxazolidinone, lincosamide, rifamycin, nitrofurans, nucleoside, antiseptic/DNA intercalation, polyether, sulfonamide, streptogramin, anti-mycobacterial, aminocyclitol, phosphonic, phenicol, and other classes with less than four antibiotics represented.

### Retraining model with validation data

To enable future model use and re-use, we trained a model on the combined primary screen data and the data from the first round of ML validation. We followed a similar hyperparameter optimization training as earlier. Grid search models were assessed based on their performance on a 10% testing set. The grid search model with best performance had the following architecture: dropout rate of 0.25, one feedforward layer, five message-passing layers, initial learning rate of 0.001, and 500 nodes in each feedforward layer. This model was predictive on the 10% test set, with a mean auROC of 0.837 and mean auPR of 0.486 predicting growth inhibition and a mean auROC of 0.904 and mean auPR of 0.402 predicting stationary-phase killing. Next, this model was evaluated on the 20% held-out test set, maintaining its high performance with an auROC of 0.941 and auPR of 0.543 on growth inhibition prediction and an auROC of 0.891 and auPR of 0.199 on stationary-phase killing prediction. Finally, we trained 30 ensemble models with 100% of the available training data with this architecture, according to the same training protocol described earlier. This final ensemble model had a growth inhibition prediction auROC of 0.894 +/- 0.066 and auPR of 0.470 +/- 0.127 and a stationary-phase killing prediction auROC of 0.844 +/- 0.078 and auPR of 0.251 +/- 0.179 over 30 folds. This model has been deposited on GitHub for re-use.

### Retrained model deployed on more diverse chemical datasets

We undertook a second round of virtual screening with the retrained model. We deployed the GNN on MolPort, ChemBridge, MayBridge, and Ambinter vendor libraries (N~5.349 million compounds) to predict growth inhibition and stationary-phase killing activity values. We carried forward only those compounds that had predicted killing scores greater than 0.1, a lenient threshold to discover unique scaffolds, leaving 12,323 molecules. We next applied strict similarity filtering, carrying forward compounds with <50% similarity to the training set and known antibiotics, leaving 6,700 molecules. To curate compounds with drug-like scaffolds, we carried forward molecules with no Egan drug-likeness violations (N=4,932), no Ghose drug-likeness violations (N=1,975), no Lipinski drug-likeness violations (N=1,675), no PAINS alerts (N=1,501), and no Brenk alerts (N=467). Hierarchical clustering was used to group compounds into clusters of similar scaffolds and a parameter sweep determined the number of clusters for which the average minimum Tanimoto similarity within each cluster was at least 50% (N=114 clusters). The highest-scoring compound was selected from each of the 114 clusters and manually annotated with a literature search. Compounds were discarded if the compound as a whole or any part of the compound had reported toxicity issues or contained known antibacterial scaffolds and antibacterial functional groups (e.g., sulfonamides, quinolines, benzimidazoles, naphthalenes, indoles). There were repeated scaffolds within the remaining 60 compounds so any compounds with a Tanimoto similarity greater than 50% to at least one other compound in the dataset were manually deduplicated. Out of the final 37 compounds, we ordered 33 compounds that were available via MolPort; we also ordered three compounds within the Broad 800K library that were at least 90% similar to one of the final 37 compounds.

### Generation of t-SNE

To generate the t-SNE in Figure S2E, the primary screen and the ML-curated compounds were split into four categories of compounds: non-hits with neither stationary-phase killing nor growth inhibition activity (N=6,699), killing activity only (N=30), growth inhibition activity only (N=92), and compounds with both killing and growth inhibition activity (N=75). The `sklearn.decomposition`<sup>115</sup> module was used to perform a PCA on RDKit Fingerprints with radius 2 and length 2,048. The PCA was performed with 2,048 components and all other defaults. Then, the PCA components were used as input to a t-SNE via `sklearn.manifold`<sup>115</sup> with two components for visualization with all defaults. For the t-SNE with the Broad 800K library (Figure S2A), a random sample (N=50,000) of the library was taken and a perplexity of 50 was used to accommodate a larger number of points. `Plotly express`<sup>116</sup> was used to make an interactive t-SNE.

### Resazurin-based cytotoxicity assays

HepG2 and HEK293 cells from ATCC were grown in Dulbecco's Modified Eagle Medium (DMEM) supplemented with 10% fetal bovine serum and 1% penicillin-streptomycin at 37°C with 5% CO<sub>2</sub> in a humidity-controlled incubator. The day before the assay, ~10<sup>4</sup> cells were plated in each well of a black polystyrene 96-well flat-bottom tissue culture-treated plate. Cells were allowed to adhere for 24 hours, then 1 μL of compound in DMSO was added for a final concentration of 10 μM for all compounds except for the second-round ML compounds, which were tested at 16 μg/mL. After 24 hours, resazurin was added to cells at a final concentration of 0.15 mM. After an additional 4 hours of incubation, fluorescence was read on a Spectramax M3 plate reader at an excitation wavelength of 550 nm and emission wavelength of 590 nm. Relative viability was calculated by dividing the fluorescence of the experimental well by the fluorescence of cells treated with a vehicle (DMSO) control. After removing cytotoxic compounds, it was discovered that one of the ML-predicted compounds, BRD-K01228321 (labeled with the SMILES string Cl[Pt]Cl in the Broad 800K Library), was misannotated. According to the Broad Chemical Biological Informatics Platform, the identity of this compound is cisplatin (SMILES: N[Pt](N)(Cl)Cl), which was evaluated in the primary screen. The duplicate was removed before evaluating metabolism dependence.

### Determination of metabolism dependence

The complete metabolism-dependence assay with semapimod (Figures 4C–4E) was performed according to Zheng et al., 2020.<sup>16</sup> Briefly, an overnight culture of Ec BW was diluted 1 in 10,000 in LB broth and grown for 4 hours. Next, cells were spun at 4,000 x g, 4°C for 15 minutes and washed with PBS three times. Cells were re-suspended in LB, PBS, or 0.1%, 1%, or 10% LB diluted in PBS and incubated for 2 hours at 37°C, then back diluted in their respective nutrient condition to approximately 10<sup>6</sup> CFU/mL. Cells were distributed into 96-well plates with two-fold dilutions of compound for a total volume of 100 μL and incubated at 37°C, 900 rpm shaking for 3 hours. Plates were washed twice in PBS, then cells were serially diluted 10-fold in PBS and 7 μL was spotted on LB agar plates for CFU enumeration. Survival data were plotted against intracellular ATP (determined in Zheng et al., 2020<sup>16</sup>) for semapimod concentrations of 2X MIC and above. As nutrient content correlates with ATP levels, this allows for a comparison of antibiotic efficacy against cells in low versus high metabolic states.<sup>16</sup> The change in survival was then divided by the change in ATP levels for each media condition (from Zheng et al., 2020<sup>16</sup>), and metabolism-dependence values were determined by performing linear regression on the survival versus ATP data and taking the negative slope. Compounds that lose efficacy in low metabolic conditions have a positive metabolism dependence, while compounds that gain efficacy in low metabolic conditions have a negative metabolism dependence.

For the high-throughput metabolism-dependence determination (Figure 3D), experiments were performed identically as described above except survival was only determined in PBS (low metabolic condition) or LB (high metabolic condition) and only at a single concentration of compound (50 μM). The change in cellular survival between LB and PBS was then divided by the change in intracellular ATP, and the negative of the resultant value was taken as the metabolism dependence. Positive metabolism-dependence values indicate that antibiotic lethality was greater in LB than PBS, whereas negative metabolism-dependence values indicate antibiotic lethality was greater in PBS than LB.

### Determination of IC<sub>50</sub>, LD99.99, and selectivity index

For stationary-phase killing dose-response assays, a minimum of eight compound concentrations were tested with a maximum concentration of 200  $\mu$ M. Ec BW cells were grown to stationary-phase in 1% LB broth diluted in PBS, then compounds were added for 24 hours, after which cells were serially diluted and plated on antibiotic-free agar for colony enumeration. HepG2 cytotoxicity dose-response assays were performed using a minimum of eight tested drug concentrations with a maximum concentration of 100  $\mu$ M using the resazurin-based cytotoxicity assay described above. Briefly, HepG2 cells were plated at  $10^4$  cells/well in DMEM with 10% fetal-bovine serum and 1% penicillin-streptomycin, and the following day compound was added and cells were incubated for another 24 hours. Next, resazurin was added and after a further 4-hour incubation period, fluorescence was read.

The IC<sub>50</sub> was determined using Graphpad Prism (version 9.4.0) using a four-parameter dose-response curve. Log-transformed CFU values were used to calculate the bacterial killing IC<sub>50</sub>. For mammalian cytotoxicity dose-response curves, if the IC<sub>50</sub> value was not achieved within the tested concentrations, it was imputed at the highest tested concentration of 100  $\mu$ M. The selectivity index was calculated by dividing the mammalian IC<sub>50</sub> by the bacterial killing IC<sub>50</sub>. During dose-response testing it was noted that micro-nomicin no longer retained killing activity, and it was removed from further consideration. The LD99.99 was determined using the equation:

$$LD99.99 = \left( \frac{F}{100 - F} \right)^{1/H} IC_{50}$$

where F is the desired response for killing four logs of stationary-phase bacteria. The Hill slope (H) and IC<sub>50</sub> inputs were determined using Graphpad Prism's four-parameter dose response curve fit.

### Red blood cell hemolysis assay

Rat Sprague Dawley red blood cells (Innovative Research) were spun at 250 x g for 5 minutes at 4°C and washed with PBS until the supernatant was clear. Cells were then re-suspended to a concentration of  $5 \times 10^8$  cells/mL in PBS and added to a 96-well clear polypropylene round-bottom plate with two-fold dilutions of compound, to a final volume of 100  $\mu$ L. 1% TritonX100 served as the positive control, and DMSO was the negative control. Plates were incubated for 1 hour at 37°C, then centrifuged at 1,500 x g for 5 minutes. Supernatants were transferred to a new plate, and the optical density at 540 nm was measured using a Spectramax M3 plate reader. Percent hemolysis was calculated by first subtracting the optical density of the negative control well from all wells, then dividing the OD<sub>540</sub> of the sample well by the OD<sub>540</sub> of the positive control.

### Growth inhibition and checkerboard assays

An overnight culture was diluted 1 in 10,000 in fresh LB and distributed into 96-well round-bottom clear polypropylene plates (Corning) with antibiotic for a total volume of 100  $\mu$ L. Plates were sealed with AeraSeal membranes (Sigma-Aldrich), then incubated for 24 hours at 37°C with 900 rpm shaking. Finally, plates were read on a Spectramax M3 plate reader (Molecular Devices) at an optical density of 600 nm.

For checkerboard assays, both antibiotics were added simultaneously in two-fold dilutions to create a checkerboard. FIC<sub>i</sub> was calculated as follows,

$$FIC_i = \frac{MIC_{AB}}{MIC_A} + \frac{MIC_{BA}}{MIC_B}$$

where MIC<sub>A</sub> and MIC<sub>B</sub> are the MIC of each antibiotic when administered individually, MIC<sub>AB</sub> is the MIC of antibiotic A in combination with antibiotic B, and MIC<sub>BA</sub> is the MIC of antibiotic B in combination with antibiotic A. If the MIC was not attained, it was imputed at two-fold the highest tested concentration. An FIC<sub>i</sub> value of <0.5 indicates synergy, a value between 0.5-4 indicates indifference, and a value >4 indicates antagonism.

### NPN membrane permeabilization assay

Ec BW was grown overnight in LB at 37°C with shaking at 300 rpm, then diluted 1:100 in LB and grown to OD<sub>600</sub> of 1 in the same conditions (3 hours). Cells were centrifuged at 4,000 rpm, 4°C for 15 minutes, washed in 5 mM HEPES buffer (Sigma-Aldrich SRE0065) with 20 mM glucose twice, and resuspended in an equal volume of the HEPES buffer. Next, cells were distributed in a 96-well clear flat-bottom black tissue-culture-treated plates (Corning 3603) with drug and 20  $\mu$ M NPN for a total volume of 100  $\mu$ L. Plates were then incubated at room temperature for 1 hour with no shaking. The fluorescence at 355/420 nm (excitation/emission) was read using a SpectraMax M3 plate reader with readings taken from the top. NPN uptake percentage was defined according to Macnair et al. (2018),<sup>82</sup> as:

$$NPN \text{ uptake (\%)} = \frac{(F_{obs} - F_0)}{(F_{max} - F_0)} \times 100\%$$

where  $F_{obs}$  is the fluorescence at a specific concentration of drug;  $F_0$  is the initial fluorescence of NPN in the absence of drug; and  $F_{max}$  is the fluorescence at the maximum concentration of the drug tested.

### Laurdan membrane fluidity assay

The membrane fluidity determination protocol was adapted from Müller et al. (2016).<sup>117</sup> Ec BW was grown overnight in LB broth at 37°C with shaking at 300 rpm, and then diluted 1:10,000 in fresh LB and grown to an OD<sub>600</sub> of 0.5 with the same conditions. One mM laurdan (Sigma-Aldrich 40227) was prepared in 100% DMF (Sigma-Aldrich PHR1553) and stored at -20°C in the dark. Next, 500 µL of the 1 mM laurdan stock was added to the cells and incubated for 5 minutes at 37°C with shaking at 300 rpm in the dark. Cells were then centrifuged at 4,000 rpm for 5 minutes, washed four times in PBS with 0.2% (w/v) glucose, then resuspended in 50 mL PBS with 0.2% (w/v) glucose. Re-suspended cells were distributed into a 96-well black clear-bottom black tissue-culture-treated plate (Corning 3603) with two-fold dilutions of semapimod. Tween-20 (Sigma-Aldrich 655204), a known membrane fluidizer,<sup>118</sup> served as the positive control, whereas untreated cells served as the negative control. Plates were incubated at 37°C for 12 minutes, then an endpoint read was taken using a SpectraMax M3 plate reader with an excitation wavelength of 330 nm and two emission readings at 460 nm and 500 nm. The laurdan generalized polarization (GP) was calculated with the formula:

$$GP = \frac{I_{460} - I_{500}}{I_{460} + I_{500}}$$

where  $I_{460}$  indicates the fluorescence intensity at 460 nm and  $I_{500}$  indicates the fluorescence intensity at 500 nm.

### Microfluidic imaging

Ec BW was grown overnight in LB at 37°C with shaking at 220 rpm, then diluted 1:1,000 in PBS containing 1% LB in an Erlenmeyer flask and grown for 24 hours in the same conditions. The following solutions were prepared fresh on the day of imaging:

- Solution 1: PBS containing 1% LB
- Solution 2: PBS containing 1% LB and SYTOX Blue (5 µM)
- Solution 3: a 1:1 mixture of cells and PBS containing 1% LB, SYTOX Blue (5 µM), and 0.2% DMSO (vehicle) or semapimod (25 µM).

The CellASIC ONIX2 platform (Merck Millipore) and the associated bacterial microfluidic plate (B04A-03) were used for microfluidic imaging, as previously described.<sup>76,107</sup> Microfluidic chambers and channels were primed with solution 1 at a flow rate corresponding to 20 kPa for 30 minutes, then loaded with solutions 2 and 3 in sequence before being transferred to a spinning disc confocal microscope for imaging. Microscopic observation was run overnight for approximately 16 hours in 5-minute intervals at 37°C on a spinning disc confocal microscope (Andor Dragonfly 200, Oxford Instruments) on a Nikon Eclipse Ti inverted microscope using brightfield and fluorescence with a 100x NA 1.45 oil objective (Nikon). Time-lapse images were analyzed using the MicrobeJ plugin<sup>119</sup> on Fiji.<sup>120</sup> Data shown are representative of 12 different fields of view spread across three biological replicates for vehicle-treated cells, and 15 different fields of view spread across three biological replicates for semapimod-treated cells.

### Semapimod evolution protocol

An overnight culture of Ec BW was diluted 1:100 in 400 µL LB in a deep 96-well plate with 0.5x, 1x, 2x, and 4x MIC of semapimod. Plates were incubated at 37°C, 900 rpm for 24 hours. The following day, the new MIC was then determined, and the culture that grew at the highest concentration of semapimod was used to inoculate fresh LB.<sup>121</sup> This process was repeated every day over the course of the evolution.

For mutation analysis, 1 mL of overnight culture was pelleted and sent to the Microbial Genome Sequencing Center (MiGS) for DNA sequencing. Libraries were prepared with the Illumina DNA Prep Kit and IDT 10bp UDI indices, and sequencing was performed on an Illumina NextSeq 2000 with 2x151 bp reads. Bcl-convert (v3.9.3) was used for demultiplexing, quality control, and adapter trimming. Reads were aligned to the *E. coli* BW25113 genome (NCBI CP009273.1) using BWA (v0.7.17).<sup>122</sup> Variants were identified using Pilon (v1.23) with default settings.<sup>123</sup> The only mutation identified was a single base pair substitution in *pmrB* of a G to an A at position 4322809 of the *E. coli* BW25113 genome, resulting in a mutation of P94Q. The sequencing data generated in this study have been deposited in the Sequence Read Archive repository under accession code PRJNA1010194. The reference *E. coli* BW25113 genome used in this study is available in the NCBI database under accession code CP009273.1.

### BODIPY-cadaverine displacement assay

Assay media containing 50 mM Tris-HCl (pH 7.4), 2.25 µM BODIPY-cadaverine, and 5.25 µg/mL of either *E. coli* LPS (Sigma-Aldrich L3129), *K. pneumoniae* LPS (Sigma-Aldrich L4268), or *P. aeruginosa* LPS (Sigma-Aldrich L9143) was added to a black 96-well non-binding plate with two-fold dilutions of the indicated antibiotic for a final volume of 100 µL. Fluorescence was immediately measured at an excitation wavelength of 580 nm and an emission wavelength of 620 nm.

### Endotoxin binding assay

Ec BW was grown overnight from single colonies in LB at 37°C with shaking at 300 rpm, then diluted 1:100 in PBS containing 1% LB and grown overnight again in the same conditions. Cells were then treated with DMSO vehicle (final concentration, 1%), colistin (final concentration, 10 µg/mL), ampicillin (final concentration, 50 µg/mL), or semapimod (final concentration, 67 µM) and incubated at 37°C with shaking at 300 rpm. After 3 hours of treatment, cells were taken out of incubation for CFU determination and cell lysate

harvesting. For CFU determination, cells were serially diluted in PBS, plated on LB agar plates, and incubated overnight at 37°C in a stationary incubator. For cell lysate harvesting, 500  $\mu$ L of each cell culture was aliquoted, and 500  $\mu$ L of B-PER II (ThermoFisher 78260) containing 100  $\mu$ g/mL lysozyme (MilliporeSigma L6876), 5 U/mL DNase (ThermoFisher 90083), and 0.2% lysonase (MilliporeSigma 71230) was added to each sample. Each sample was then incubated at 37°C for 30 minutes for harvesting. Samples were centrifuged at 3,720  $\times$  g for 10 minutes and the supernatant was collected. Protein concentration was measured using the Pierce BCA protein assay following the manufacturer's instructions, and endotoxin concentration was measured using the LAL endotoxin quantification kit.

Briefly, Pierce BCA protein reagent was prepared by mixing reagents A and B at a 50:1 ratio. Next, 200  $\mu$ L of reagent was mixed with 25  $\mu$ L of sample in a 96-well clear flat-bottom plate, and samples were incubated for at least 30 minutes at 37°C. The absorbance at 562 nm was read using a SpectraMax M3 plate reader, and protein concentrations in samples were quantified by interpolating with respect to a standard curve generated from standards containing 2,000, 1,500, 1,000, 750, 500, 250, 125, 25, and 0  $\mu$ g/mL BSA in PBS. The protein concentration of the B-PER II solution was subtracted from each sample in order to determine the protein concentration arising from bacterial cells.

For endotoxin quantification, endotoxin standards, LAL reagent, and chromogenic substrate were suspended in endotoxin-free water, and 50  $\mu$ L of each sample was reacted with 50  $\mu$ L of LAL reagent for 10 minutes at 37°C in a 96-well clear flat-bottom plate. Then, 100  $\mu$ L of chromogenic substrate was added to each reaction. After a final incubation step of at least 6 minutes, the absorbance was read at 410 nm. Endotoxin concentrations in samples were quantified by interpolating or extrapolating with respect to a standard curve generated from standards containing 1, 0.5, and 0 endotoxin units (EUs) diluted in PBS.

### Thermal proteome profiling (TPP)

Ec BW was grown in LB overnight at 37°C with shaking at 300 rpm, and then diluted 1:2,000 and grown to an OD<sub>600</sub> of 0.5. Cells were then spun at 4,000  $\times$  g for 5 minutes and resuspended in PBS, followed by lysis on ice in buffer containing 0.8% IGEPAL CA-630 (Sigma-Aldrich I3021-50ML), 50  $\mu$ g/ml lysozyme (Sigma-Aldrich L6876-5G), 1X Halt protease inhibitor (Life Technologies 87786), 250 U/ml benzonase (Sigma-Aldrich E1014-25KU), and 1 mM MgCl<sub>2</sub>. The lysate was divided and incubated with 10  $\mu$ M semapimod or an equivalent volume of DMSO for 20 minutes at room temperature with gentle agitation. The lysates were split into 120  $\mu$ L aliquots in PCR tubes and heated at the following temperatures on two 48-well heat blocks: 40°C, 43.5°C, 47°C, 51.3°C, 54.9°C, 58°C, 60.4°C, 62.5°C, 65.6°C, and 70°C. After 3 minutes, the tubes were removed from the heat blocks and were chilled on ice for 5 minutes. The lysates were transferred to a TLA-100 rotor and spun at 100,000  $\times$  g for 20 minutes at 4°C in a Beckman Ultra MAX benchtop ultracentrifuge. The soluble protein fraction was separated from the pellet for further processing.

To perform protein cleanup and digestion, concentrations of the 40°C samples were determined with a DC Protein Assay (BioRad 5000116). A volume corresponding to 50  $\mu$ g of the 40°C sample was used for further analysis. Equivalent volumes were used from the remaining temperature range samples. Samples were prepared using a modified version of the SP3 protocol.<sup>92,124</sup> Proteins were reduced with 5 mM Tris(2-carboxyethyl)phosphine (TCEP, Pierce 20490) for 20 minutes at 50°C, and cysteines were alkylated with 15 mM MMTS (Thermo Fisher Scientific 23011) for 10 minutes at room temperature. Next 500  $\mu$ g of a 1:1 mix of hydrophobic and hydrophilic beads (GE Healthcare 65152105050250 and 45152105050250) was added to each sample, followed by a 6x volume of 100% ethanol to induce bead aggregation. The samples were agitated at 1,000 rpm on a thermomixer for 10 minutes at room temperature. The beads were magnetically separated, and the supernatant was removed. The beads were washed three times with 80% ethanol and were then resuspended in 35  $\mu$ L of 50 mM TEAB (Sigma-Aldrich T7408-100ML) with 2  $\mu$ g trypsin/LysC protease mix (Thermo Fisher Scientific A40007). Digestion was performed for 16 hours at 37°C and 1,000 rpm. Peptides were separated from the bead supernatant using a Dynamag<sup>TM</sup>-2 magnet (Thermo Fisher Scientific 12321D).

Peptides were TMT10plex-labeled according to the manufacturer's protocol (Thermo Scientific 90111), with the following modifications. Approximately 35  $\mu$ L of eluate was combined with 100  $\mu$ g of TMT10plex reagent (Thermo Fisher Scientific 90110) in 15  $\mu$ L of acetonitrile, for an estimated 1:2 w/w peptide:tag labeling reaction. The labeling proceeded for 1 hour at room temperature and was quenched for 15 minutes with 5% hydroxylamine (Thermo Fisher Scientific 90115). The samples were then pooled, flash-frozen, and lyophilized to dryness. Samples were fractionated with the Pierce High pH Reversed-Phase Peptide Fractionation Kit (Thermo Fisher Scientific 84868), according to the manufacturer's instructions for TMT-labeled peptides, followed by lyophilization to dryness.

To acquire mass spectrometry data, the fractions were lyophilized and resuspended in 20  $\mu$ L of 0.1% formic acid (Thermo Fisher Scientific 28905) and were analyzed on an Exploris 480 Orbitrap mass spectrometer equipped with a FAIMS Pro source<sup>125</sup> connected to an EASY-nLC chromatography system. Peptides were loaded onto a 25 cm EasySpray nanoLC column (Thermo Fisher Scientific ES902) guarded by a 2 cm Acclaim PepMap 100 guard column (Thermo Fisher Scientific 164946) using an injection volume of 1  $\mu$ L. The analytes were separated at 300 nl/minute on a gradient of 1–25% B for 90 minutes, 25–40% B for 30 minutes, 40–95% B for 10 minutes, 95% B for 10 minutes, and a seesaw gradient of 95–2% B for 2 minutes, 2% B for 2 minutes, 2–98% B for 2 minutes, 98% B for 2 minutes, 98–2% B for 2 minutes, and 2% B for 2 minutes. The orbitrap and FAIMS were operated in positive ion mode with a positive ion voltage of 1800V; with an ion transfer tube temperature of 270°C; using standard FAIMS resolution and compensation voltages of -50V and -65V; and an inner and electrode temperature of 100°C with 4.6 ml/minute carrier gas. Full scan spectra were acquired in profile mode at a resolution of 120,000, with a scan range of 350–1200 m/z, automatically determined maximum fill time, standard AGC target, intensity threshold of 5  $\times$  10<sup>3</sup>, 2–5 charge state, and dynamic exclusion of 30 seconds with a cycle time of 2

seconds between master scans. MS2 spectra were generated with a HCD collision energy of 36 at a resolution of 30,000 using TurboTMT settings with a first mass at 110 m/z, an isolation window of 0.7 m/z, standard AGC target, and auto injection time.

Raw data files were analyzed in Proteome Discoverer 2.4 (Thermo Fisher Scientific) to generate peak lists and protein and peptide IDs using Sequest HT (Thermo Fisher Scientific) and the *E. coli* K12 (Uniprot UP000000625) protein database. The search included the following post-translational modifications: dynamic phosphorylation (+79.966 Da; S, T, Y), dynamic oxidation (+15.995 Da; M), static TMT6plex (+229.163 Da; any N-terminus), static TMT6plex (+229.163 Da; K), and static methylthio (+45.988 Da; C). Reporter quantification was performed on ions with an average S/N over 10 and co-isolation threshold of 50%. Protein-level quantification was determined from unique peptides only. Normalization was turned off. Otherwise, default settings were used. The mass spectrometry proteomics data have been deposited to the ProteomeXchange Consortium via the PRIDE<sup>126</sup> partner repository with the dataset identifier PXD044230 (<https://www.ebi.ac.uk/pride/archive/projects/PXD044230>). TMT reporter ion Abundance ratios relative to the lowest-temperature sample were used as input to the TPP package<sup>91</sup> for normalization and curve fitting in R version 4.0.4.<sup>127</sup> P-values were calculated using the `analyseTPPTR` function within Bioconductor's TPP package using the 'RobustZ' method.<sup>128</sup> Overexpression strains were sourced from the ASKA library.<sup>129</sup> Knockout strains were sourced from the KEIO library.<sup>130</sup>

### QUANTIFICATION AND STATISTICAL ANALYSIS

The number of biological replicates and meaning of error bars can be found in the figure legends. Unless otherwise specified, significance was determined with a value of  $p < 0.05$ .